Advanced Review

# Natural bond orbital methods

Eric D. Glendening,[1] Clark R. Landis[2]* and Frank Weinhold[2]

Natural bond orbital (NBO) methods encompass a suite of algorithms that enable fundamental bonding concepts to be extracted from Hartree-Fock (HF), Density Functional Theory (DFT), and post-HF computations. NBO terminology and general mathematical formulations for atoms and polyatomic species are presented. NBO analyses of selected molecules that span the periodic table illustrate the deciphering of the molecular wavefunction in terms commonly understood by chemists: Lewis structures, charge, bond order, bond type, hybridization, resonance, donor–acceptor interactions, etc. Upcoming features in the NBO program address ongoing advances in *ab initio* computing technology and burgeoning demands of its user community by introducing major new methods, keywords, and electronic structure system/NBO communication enhancements.  *WIREs Comput Mol Sci* 2011 00 1–42 DOI: 10.1002/wcms.51

## INTRODUCTION

'Natural bond orbital (NBO) methods' refers to a suite of mathematical algorithms for analyzing electronic wavefunctions in the language of localized Lewis-like chemical bonds. In these methods, molecular properties are expressed in terms of a 'natural Lewis structure' (NLS) depiction of the wavefunction, in direct correspondence to the elementary Lewis dot diagram of freshman chemistry. Each one-center (1c) lone pair or two-center (2c) bond pair of the Lewis structure diagram is thereby associated with a 'Lewis' (L type) member of the complete orthonormal set of NBOs, whereas remaining 'non-Lewis' (NL type) NBOs describe residual resonance delocalization effects (departures from idealized L-type representation). NBOs can be described as a 'chemist's basis set' that allows any aspect of the wavefunction to be expressed in terms of L- versus NL-type contributions, thereby providing a bridge between modern wavefunction technology and elementary valency and bonding concepts. (We focus initially on simple closed-shell species, but the easy generalization to open-shell systems is illustrated in examples to follow.)

The aptness and efficiency of NBO-based wavefunction description testifies to the profound conceptual insights of G. N. Lewis as well as associated hybridization and resonance concepts of G. N. Lewis, L. Pauling, J. C. Slater, and C. A. Coulson.[1–4] The optimal mathematical properties of localized NBOs trace their heritage to the general mathematical theory of 'natural' orbitals (eigenorbitals of the first-order reduced density operator) as originally expounded by P.-O. Löwdin[5] and outlined below. The mathematical and historical background of NBO methods is described more completely in a comprehensive research monograph.[6]

## OVERVIEW: WHAT ARE NATURAL BOND ORBITALS?

The key distinguishing feature of NBOs is their formulation in terms of *natural atomic orbitals* (NAOs), a complete orthonormal set for optimally describing the effective *atom*-like constituents within the molecular environment. At large interatomic separations, the NAOs $\{\theta_i^{(A)}\}$ essentially reduce to the corresponding atomic natural orbitals[7] (ANOs) of isolated atoms. However, in a given molecular environment, the NAOs reflect the chemical give and take of electronic interactions, with variations of shape (e.g., angular deformations due to steric pressures of adjacent atoms) and size (e.g., altered diffuseness due to increased anionic or cationic character) that distinguish them appreciably from free-atom forms. Given an effective one-electron Hamiltonian **F** (e.g., Fock or Kohn–Sham operator) for the system, with associated NAO orbital energies $\varepsilon_i^{(A)}$,

$$\varepsilon_i^{(A)} = \langle \theta_i^{(A)} | \mathbf{F} | \theta_i^{(A)^*} \rangle, \qquad (1)$$

*Correspondence to: landis@chem.wisc.edu

[1]Department of Chemistry and Physics, Indiana State University, Terre Haute, IN, USA

[2]Department of Chemistry, University of Wisconsin, Madison, WI, USA

DOI: 10.1002/wcms.51

  

one can formally construct the effective atomic Hamiltonian $\mathbf{h}^{(A)}$ of each atom in matrix–algebraic ket-bra (integral operator kernel) form as

$$\mathbf{h}^{(A)} = \sum_i \varepsilon_i^{(A)} \left|\theta_i^{(A)}\right\rangle\left\langle\theta_i^{(A)}\right|. \tag{2}$$

NAOs thereby provide the starting point for perturbative dissection of system properties into intra-atomic ($\mathbf{h}^{(A)}$) and interatomic ($\mathbf{V}_{int}$) contributions, viz.,

$$\mathbf{F} = \sum_A \mathbf{h}^{(A)} + \mathbf{V}_{int}. \tag{3}$$

The NAO-based model atomic Hamiltonian $\mathbf{h}^{(A)}$ allows convenient description of NBO formation and interactions in simple perturbative terms, as will be illustrated below.

The NAOs also underlie *natural population analysis* (NPA),[8] the 'natural' quantification of orbital population ($q_i^{(A)}$) and atomic charge ($q^{(A)}$) at each atomic center A. Such quantities are simply evaluated as

$$q_i^{(A)} = < \theta_i^{(A)} | \Gamma^{(1)} | \theta_i^{(A)} >, \tag{4a}$$

$$q^{(A)} = Z_A - \sum_i q_i^{(A)}, \tag{4b}$$

where $\mathbf{\Gamma}^{(1)}$ is the first-order reduced density operator[5] of the overall system and $Z_A$ is the atomic number of atom A. Although many alternative charge partitionings have been suggested (going back to original Mulliken population analysis[9]), the NPA populations satisfy the important physical constraints of the Pauli principle

$$0 \le q_i^{(A)} \le 2 \tag{4c}$$

and charge additivity

$$\sum_{i,A} q_i^{(A)} = N \,(\text{total number of electrons}) \tag{4d}$$

that insure overall probability conservation and consistent assignments of 'charge transfer' between atoms. NPA charge assignments are also found to exhibit excellent numerical stability with respect to variations of basis extension and wavefunction form,[10] as well as gratifying agreement with empirical structure–function relationships and other well-known measures of charge distribution in physical organic chemistry.[11]

In constrast to contracted Gaussian-type orbitals (CGTOs), Slater-type orbitals (STOs), or other 'atomic orbital' basis functions in common usage, the NAOs are most strongly distinguished by their *strict maintenance of intra- and interatomic orthonormality*. Indeed, such orthonormality

$$< \theta i^{(A)} | \theta j^{(B)} > = \delta_{ij}\delta_{AB} \tag{5}$$

is an elementary mathematical prerequisite for eigenorbitals of any physical Hermitian operator.[12] Conventional atomic orbital (AO) basis functions commonly harbor overlap of both intra- and interatomic types, corresponding to absence of proper nodal features with respect to both inner core shells on the same atom and filled core/valence shells on adjacent atoms. The nodeless character of common AOs implies violations of the Pauli exclusion principle that may be described as unrealistic 'core penetration' within the atom and 'vanishing steric pressure'[13] between atoms, leading to unphysical energetics and mixing patterns as compared to NAOs. [Further aspects of unphysical AO behavior in wavefunction analysis are described in Ref 6, p. 566ff, and www.chem.wisc.edu/~nbo5/tut_cmo (part II).]

All NBO-based constructs ultimately stem from the first-order reduced density operator $\mathbf{\Gamma}^{(1)}$, which expresses the underlying wavefunction $\Psi$ in the 'reduced' form appropriate for evaluating density and other one-electron properties.[14] By definition, natural orbitals (NOs) arise as *eigenorbitals* $\{\theta_i\}$ of $\mathbf{\Gamma}^{(1)}$:

$$\mathbf{\Gamma}^{(1)}\theta_i = q\theta_i \,(= 1, 2, \ldots) \tag{6}$$

with associated 'occupancy' eigenvalues $q_i$

$$q_i = < \theta_i | \mathbf{\Gamma}^{(1)} | \theta_i > \tag{7}$$

limited by the Pauli exclusion principle ($0 \le q_i \le 2$). General min–max properties of Hermitian eigenvalue problems allow one to alternatively define NOs as *maximum occupancy* orbitals, intrinsically optimal for expressing $\Psi$ (or associated density $\rho$) in most compact possible form. For single-determinant wavefunctions, NOs (eigenfunctions of $\mathbf{\Gamma}^{(1)}$) are equivalent to Molecular Orbitals (MOs) (eigenfunctions of $\mathbf{F}$), with degenerate occupancies

$$\begin{aligned} q_i = {} & 2\,(\text{all } i \le N/2; \text{'occupied'}) \\ & \text{or } 0\,(\text{all } i > N/2; \text{'virtual'}). \end{aligned} \tag{8}$$

However, for more general $\Psi$ the maximum-occupancy NOs must be clearly distinguished from minimum-energy MOs, and $\mathbf{\Gamma}^{(1)}$ must similarly be distinguished from the corresponding Fock–Dirac density operator of MO theory (equivalent in Hückel theory to the Coulson charge and bond-order matrix).

On chemical grounds, one expects that orbitals of near-maximal 'electron pair' occupancy ($q_i = 2$) are effectively concentrated in *localized* one-center 'lone pair' or two-center 'bond pair' regions of the

  

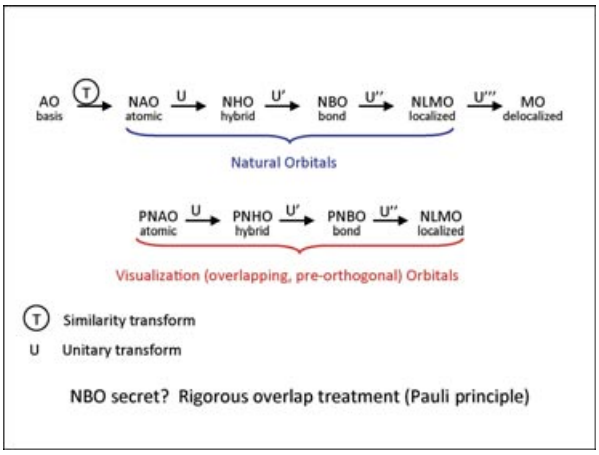


**FIGURE 1** | Overview of orthogonal and nonorthogonal basis sets underlying natural bond orbital (NBO) methods.

elementary Lewis structure diagram. Based on this expectation (and expressed somewhat heuristically), one can therefore restrict the search to *localized* high-occupancy 1c/2c regions to obtain corresponding optimal local-eigenvector orbitals of NBO type, searching over all possible bonding patterns for the best possible NLS description. Unlike conventional NOs or MOs, whose degenerate occupancies (8) lead to essential *in*determinacy up to arbitrary unitary transformation, the occupancies of NBOs are generally *distinct*, reflecting their exquisite dependence on the chemical environment. Accordingly, the localized NBOs exhibit *uniqueness* properties not shared by their delocalized NO/MO counterparts.

Figure 1 displays a glossary of acronyms and overview of mathematical relationships for various localized and delocalized orbital sets to be discussed below. The arrows depict the heirarchical sequence of similarity or unitary transforms that lead from initial AO basis functions to final delocalized MOs through various NAO-based localized sets. However, rather than focus on mathematical and algorithmic details[15] or a survey of current literature applications (currently numbering over 1000/year),[16] we shall attempt to characterize NBO methods by introducing each orbital set of Figure 1 in terms of its operational applicability to chemical systems of increasing chemical complexity, ranging from simple atomic (F, O) and diatomic [hydrogen fluoride (HF), $^3O_2$] species to more complex polyatomic molecules ($NH_2CHO$, $WH_6$, HWWH) and supramolecular complexes. [$F_3^-$, $(HF)_2$]. In this manner, we can systematically 'build up' the heirarchy of NBO-based methods and acronyms according to increasing demands of multicenter complexity.

## HOW NBO METHODS WORK IN ELEMENTARY CHEMICAL SPECIES

The general object of NBO methods is to translate accurate calculations into chemical insights. Such insights are formulated in terms of commonly understood bonding concepts such as

- atomic charge,
- Lewis structure,
- bond type (covalent vs. dative vs. ionic; $\sigma$ vs. $\pi$, etc.),
- hybridization,
- bond order,
- charge transfer,
- resonance weights,
- sterics,
- energy decomposition analysis (EDA), and
- spectroscopic descriptors (e.g., of NMR chemical shielding or J-coupling).

We now wish to illustrate how NBO methods provide effective links to these and other elementary valency and bonding concepts in simple atomic, diatomic, and polyatomic species.

### Atoms

For atomic species, immediate connections can be drawn between 'effective minimal basis' MO models and the forms and occupancies of NAOs. Although accurate *ab initio* calculations commonly require highly extended AO basis sets, the equivalent NAO basis reveals that *only a small subset of core and valence levels* carry significant occupancy, consistent with the hydrogen-like single configuration picture. In the ground-state fluorine atom, for example, one expects the five minimal-basis orbitals (viz., core 1s and valence 2s, $2p_x$, $2p_y$, $2p_z$) to adequately describe the nominal $(1s)^2(2s)^2(2p)^5$ configuration. A typical AO basis of respectable accuracy (e.g., 6–311++G**, with 22 AOs) exhibits significant Mulliken populations in *many* additional AOs, whereas the corresponding NAO populations conform superbly to the minimal basis picture, as seen in the 'natural population analysis' section of NBO output (Figure 2). Under the 'Type(AO)' column in Figure 2, one finds that labeled 'Cor' (core) and 'Val' (valence) NAOs of the 'natural minimal basis' (NMB) account for virtually *all* the electron density (99.98% according to the NPA summary in Figure 3), whereas the remaining 17 'Ryd' (extravalence Rydberg-type) NAOs are

  

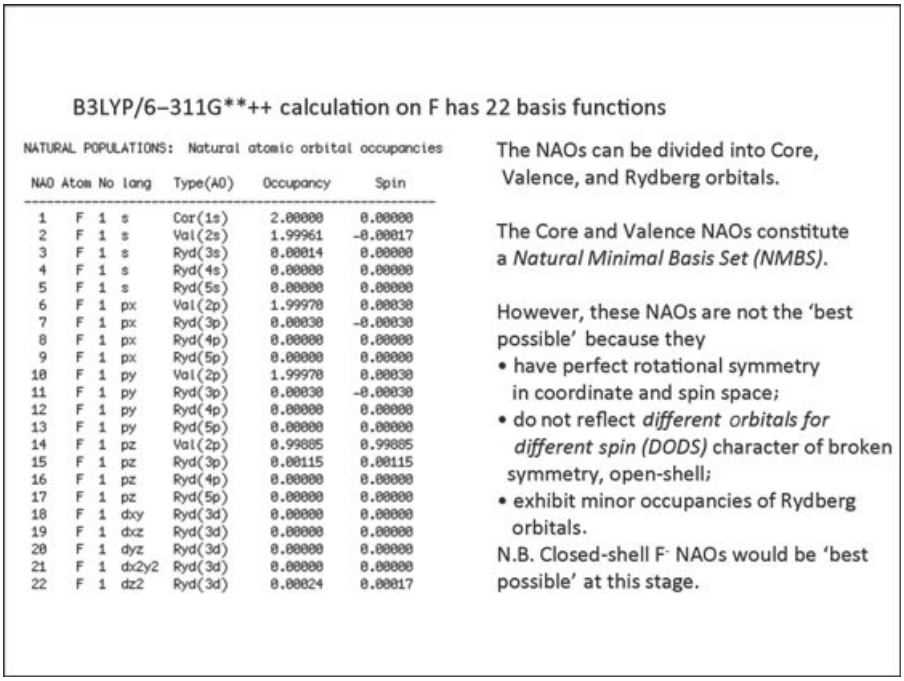


**FIGURE 2** | NAO output for F atom (all calculations at B3LYP/6–311++G** theory level unless otherwise noted.)

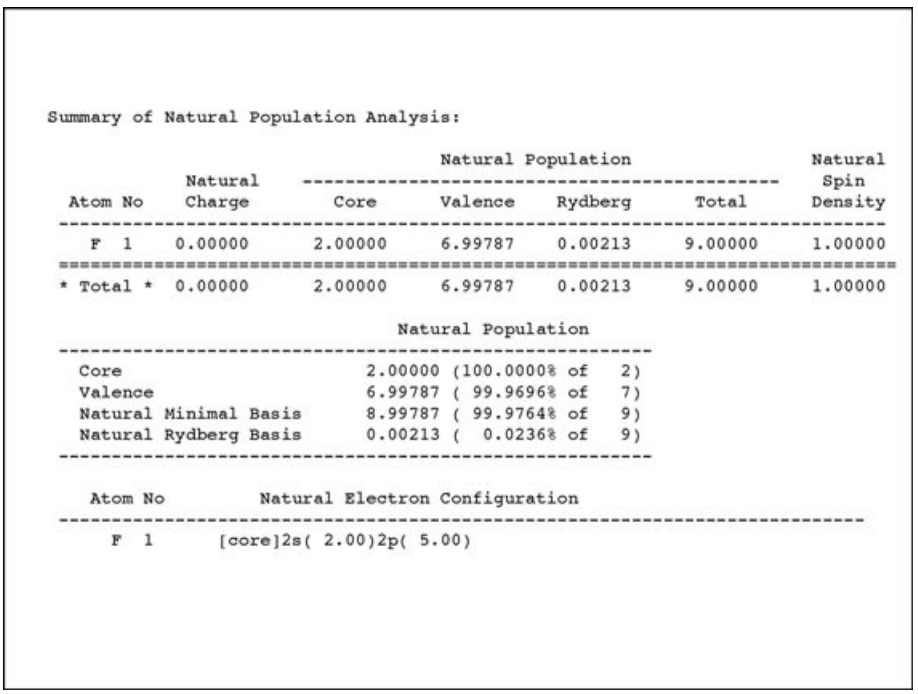


**FIGURE 3** | Natural population analysis (NPA) summary output for F atom.

essentially *ignorable* for qualitative conceptual purposes. Such extreme condensation of electron density into the small NMB set is typically maintained in molecular species of arbitrary complexity (and basis sets of arbitrary extension), vindicating key assumptions that underlie semiempirical MO models.[17]

The shapes of NAOs also conform closely to the idealized hydrogen-like forms implied by their labels, with strict rotational invariance in coordinate and spin space. However, an open-shell species such as the F atom necessarily exhibits *un*equal occupancies in both (x, y, z) coordinate space and ($\alpha$, $\beta$)

  

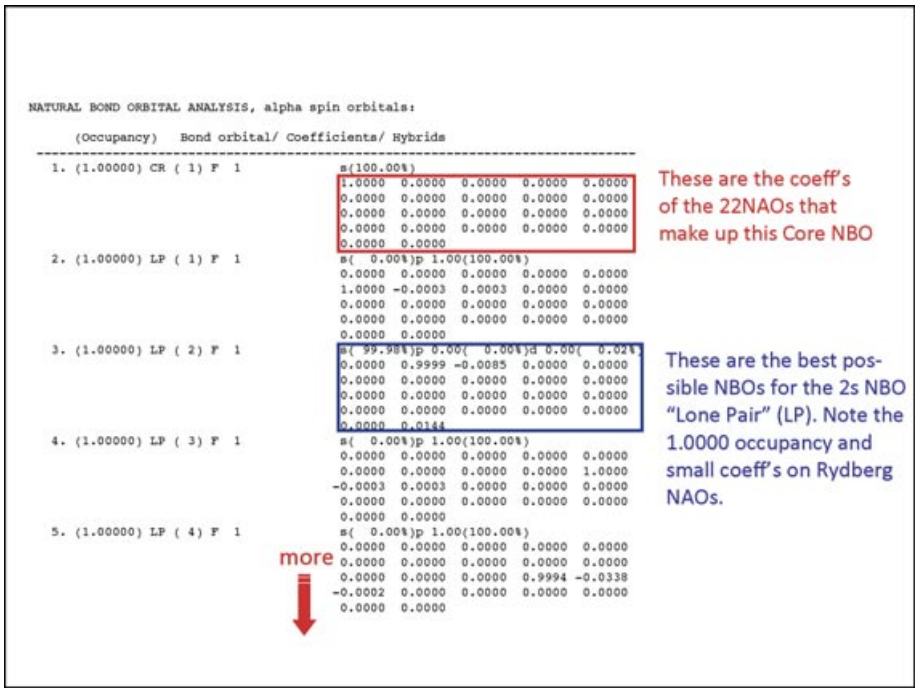


**FIGURE 4** | Natural bond orbital (NBO) listing with natural hybrid orbital (NHO) compositions and natural atomic orbital (NAO) coefficients, for alpha (majority spin) NBOs of F atom.

spin space, leading to the intrinsic broken symmetry of UHF-type wavefunctions (viz., the virtually complete isolation of spin density in the $2p_z$ NAO; Figure 2). The search for optimal NBOs (equivalent to the UB3LYP MOs in this simple case) must therefore reflect the inherent 'different orbitals for different spins' (DODS) character of the aymmetric spin distribution.[18] Figures 4 and 5 display NBO output for compositional and energetic details for spin-NBOs of $\alpha$ (majority) spin. Each $\alpha$-NBO, like the corresponding $\alpha$-MO but unlike the 'parent' NAO, has achieved maximal (unit) occupancy permitted by the Pauli principle. The boxed Linear Combination of Natural Atomic Orbitals (LCNAO)-NBO mixing coefficients in Figure 4 show the slight compositional asymmetries in each 'LP'-type NBO ('lone particle' in this open-shell case), while the NBO energy values in Figure 5 show the corresponding spatial symmetry breaking in the direction of unpaired spin. The DODS character of open-shell NBOs may initially seem puzzling, but it mirrors the corresponding broken symmetry of $\alpha$- versus $\beta$-spin MOs and expresses important physical features of open-shell electronic distribution and energetics.

To illustrate how NBO output displays DODS features of open-shell species, we can examine some puzzling aspects of Hund's rule[19] for the singlet–triplet energy difference in the oxygen atom. As is well known, many computational methods reproduce the correct energy ordering for low-lying $^1$D, $^3$P states of atomic oxygen, with triplet below singlet in accordance with Hund's rule. However, Hund's rule is usually rationalized in terms of the reduced electron–electron repulsions of the triplet state, because the Pauli principle prevents electrons of the same spin from occupying the same spatial orbital.[20] Is this a correct physical picture of the O atom singlet–triplet splitting?

In Hartree–Fock or Kohn–Sham DFT, electron–electron repulsions are represented (in mean-field approximation) by an operator **R** that can be expressed in terms of kinetic energy (**K**), nuclear–electron attraction (**V**), and overall Fock (**F**) matrix elements as

$$\mathbf{R}^{(\alpha)} = \mathbf{F}^{(\alpha)} - \mathbf{K}^{(\alpha)} - \mathbf{V}^{(\alpha)}, \tag{9a}$$

$$\mathbf{R}^{(\beta)} = \mathbf{F}^{(\beta)} - \mathbf{K}^{(\beta)} - \mathbf{V}^{(\beta)} \tag{9b}$$

for $\alpha$ and $\beta$ spin, respectively. Overall electron–electron repulsions $V_{ee}$ are therefore evaluated by tracing over the repulsions in each spin set, viz.,

$$V_{ee} = \mathrm{Tr}(\mathbf{R}^{(\alpha)}) + \mathrm{Tr}(\mathbf{R}^{(\beta)}) \tag{10}$$

Somewhat surprisingly (for adherents of the usual rationalization of Hund's rule), evaluation of (10) for $^3$P and $^1$D states of the O atom gives (e.g., at

  

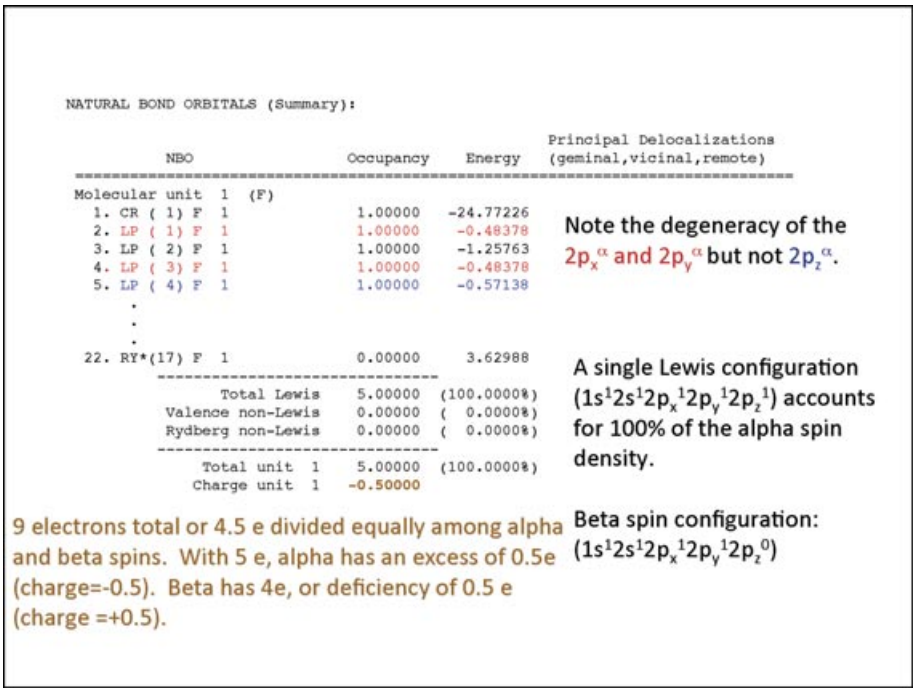


**FIGURE 5** | Natural bond orbital (NBO) Summary output for alpha-spin NBOs of F atom.

UHF/6–311++G** level)

$$^3V_{ee} = 22.8243\,\text{a.u.} \tag{11a}$$

$$^1V_{ee} = 22.7580\,\text{a.u.} \tag{11b}$$

showing that electron–electron repulsions are actually *reduced* in $^1$D compared to $^3$P. What's going on here?

NBO keyword options make it easy to obtain matrix elements of any 1e operator (O) in any chosen basis set (BAS) by the corresponding OBAS keyword. Thus, with the help of keywords FNBO (for **F**), KNBO (for **K**), and VNBO (for **V**), one can readily obtain the NBO matrix elements that allow one to track down the differences in (11a,b). Figure 6 displays numeric NBO output for the 2p-subblocks of matrices in (9a,b) that lead to the final traced differences in (10) and (11a,b). From these matrix elements one can see that

$$\begin{aligned}\text{Tr}(^3\mathbf{F}) - \text{Tr}(^1\mathbf{F}) &= 2.5536 - 2.4858 \\ &= 0.0678\,\text{a.u.},\end{aligned} \tag{12a}$$

$$\begin{aligned}\text{Tr}(^3\mathbf{K}) - \text{Tr}(^1\mathbf{K}) &= 10.1771 - 10.0981 \\ &= 0.0790\,\text{a.u.},\end{aligned} \tag{12b}$$

$$\begin{aligned}\text{Tr}(^3\mathbf{V}) - \text{Tr}(^1\mathbf{V}) &= -35.5550 - (-35.3419) \\ &= -0.2131,\end{aligned} \tag{12c}$$

showing that *increased nuclear–electron attraction* (12c) is primarily responsible for the favored triplet energy lowering. This would be quite difficult to explain in a picture that did not allow the 2p$^\alpha$, 2p$^\beta$ spin-orbitals to adopt *different* radial diffuseness, thereby allowing 'inner' 2p electrons to achieve the stabilization of enhanced nuclear–electron attraction, despite the somewhat greater electron–electron repulsions associated with radial contraction.

Of course, in the present case similar conclusions might be drawn by examining MO matrix elements, because atomic MOs and NBOs are essentially identical. In more complex chemical species, however, MOs and NBOs differ profoundly, and only the NBO matrix elements exhibit the necessary transferability (associated with freedom from arbitrary unitary transformations that plague MO theory) to allow easy extrapolation of the foregoing 1c arguments to more complex species.

## Diatomics

Although NAOs and NBOs (as well as MOs and NOs) are practically indistinguishable in atoms, formation of a diatomic molecule leads to the key orbital transformation (cf. Figure 1)

$$\text{NAO} \rightarrow \text{NHO} \rightarrow \text{NBO} \tag{13}$$

  

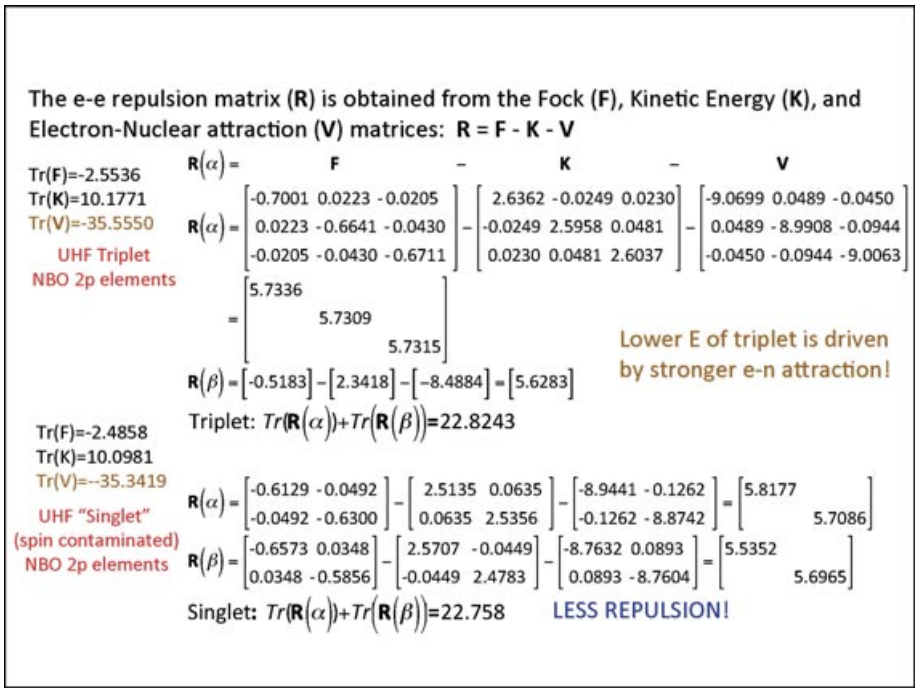


**FIGURE 6** | Natural atomic orbital (NAO) Fock (**F**), kinetic (**K**), 1e-potential (**V**), and e–e repulsions (**R**) matrices for lowest singlet and triplet states of O atom (UHF level), showing electronic origin of Hund's rule in **V** (not **R**) differences in the two states.

to form orthonormal *natural hybrid orbitals* (NHOs) as building blocks for final NBOs. Figure 7 summarizes how empirical valency ('combining power') relationships for main-group species led to powerful prequantal Lewis structural concepts based on the octet rule and electron pair bonding, which in turn were expressed quantum mechanically in terms of directed hybrid orbitals and conjectured forms of the 'valence bond' functions. The NBO transformations (13) closely mimic the historical sequence (Figure 6) for the bond orbital formulation advocated by Mulliken and others,[21,22] rather than the Heitler–London-type formulation advocated by Pauling.[23,24] Thus, the NBO algorithms bear unmistakable parallels to Pauling's valence bond (VB) theory concepts, but differ sharply in key mathematical details (often obscured by empirical VB approximations).

We can illustrate how NBO formation parallels Lewis/Mulliken bond-formation concepts for the simple case of HF molecule, as displayed in the NBO output of Figures 8–11. Near the top of Figure 8, we can see that the NBO search finds an optimal NLS having one CR (core), one BD (bond), and three LP (lone) pairs, consistent with the elementary Lewis structure diagram. The five 'Lewis NBOs' of this structure account for more than 99.95% of the total electron density, testifying to the high numerical accuracy of the qualitative concepts sketched in Figure 8. (Of course, for diatomic species the MOs and NBOs are closely related perforce, but similarly high accuracy of the Lewis-like description persists in more complex species.) Figure 9 illustrates how large off-diagonal couplings in the NAO-based density matrix (obtained with DMNAO keyword) are transformed to near-diagonal 'electron pair' occupancies in the NBO basis (DMNBO keyword). Further details of valence NBOs are presented in Figure 10, showing, e.g., that the $\sigma_{HF}$ BD orbital (with occupancy 2.00000) can be written in Mulliken form as

$$\begin{aligned}\sigma_{HF} &= c_F h_F + c_H h_H \\ &= 0.8813^*(sp^{3.90})_F + 0.4726^*(s)_H \end{aligned} \quad (14a)$$

using conventional $sp^\lambda$ notation for valence hybrids (NHOs)

$$h_F(sp^\lambda) = (1+\lambda)^{-1/2}[s_F + \lambda^{1/2} p_F]. \quad (14b)$$

Here, $\lambda$ merely expresses the percentage p-character (%-p) or s-character (%-s) of the hybrid,

$$\begin{aligned}\%-p &= 100^*\lambda/(1+\lambda), \\ \%-s &= 100/(1+\lambda), \end{aligned} \quad (14c)$$

which inherently ranges continuously from pure s ($\lambda = 0$) to pure p ($\lambda = \infty$) (even if beginning students are sometimes only taught about integer values $\lambda = 1$, 2, and 3!). The complete hybrid specification

  

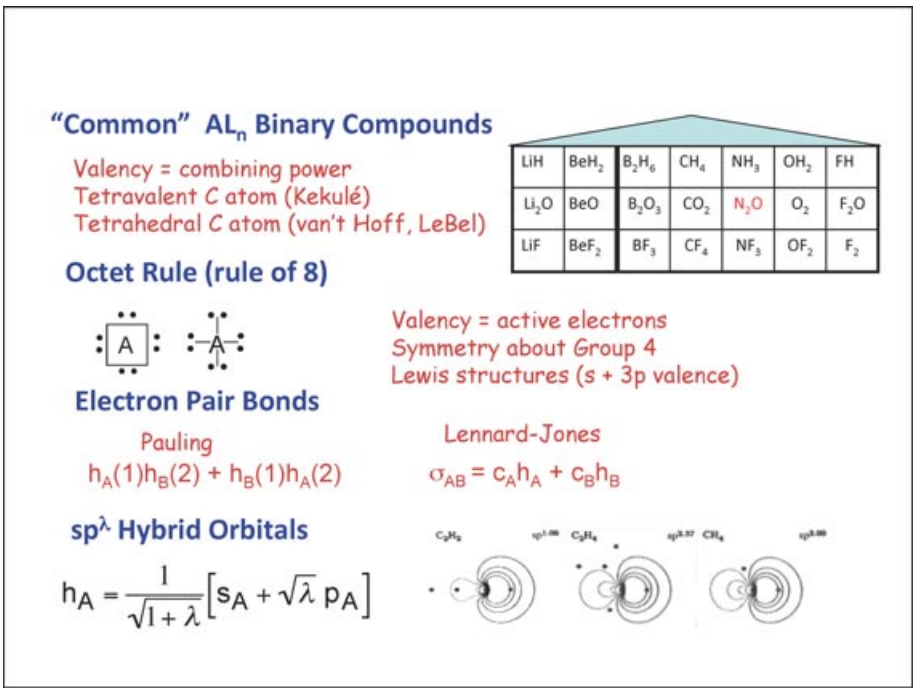


**FIGURE 7** | Overview of main-group valency, hybridization, and bonding principles, showing Lewis-like 'octet rule' and electron-pair functions as formulated by Pauling (Heitler–London valence bond) or Lennard–Jones (bond orbital).

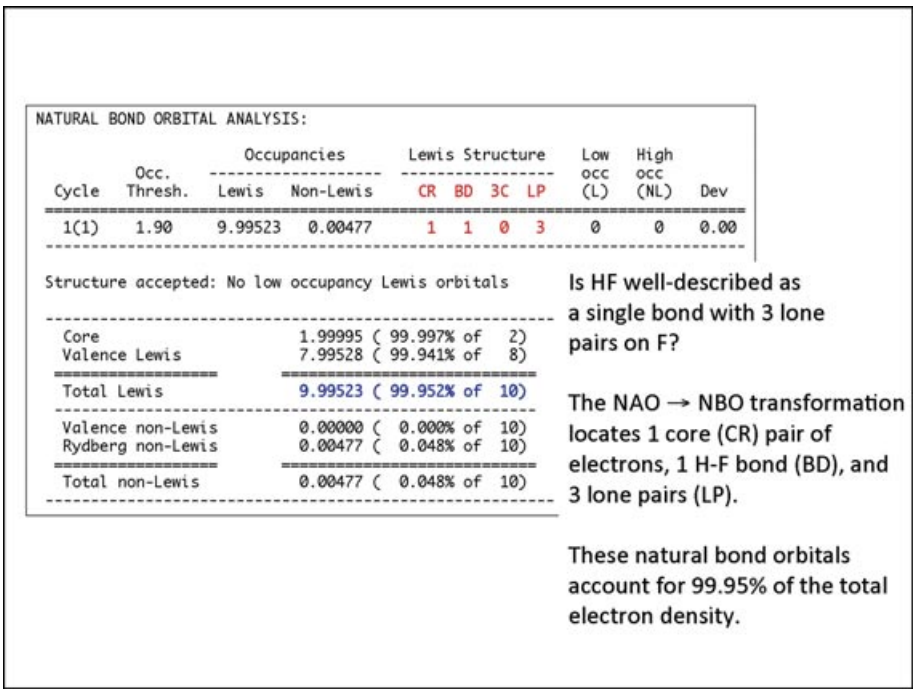


**FIGURE 8** | Natural bond orbital (NBO) search summary for hydrogen fluoride (HF) molecule, showing high accuracy (>99.95%) of Lewis-type 'natural Lewis structure' description.

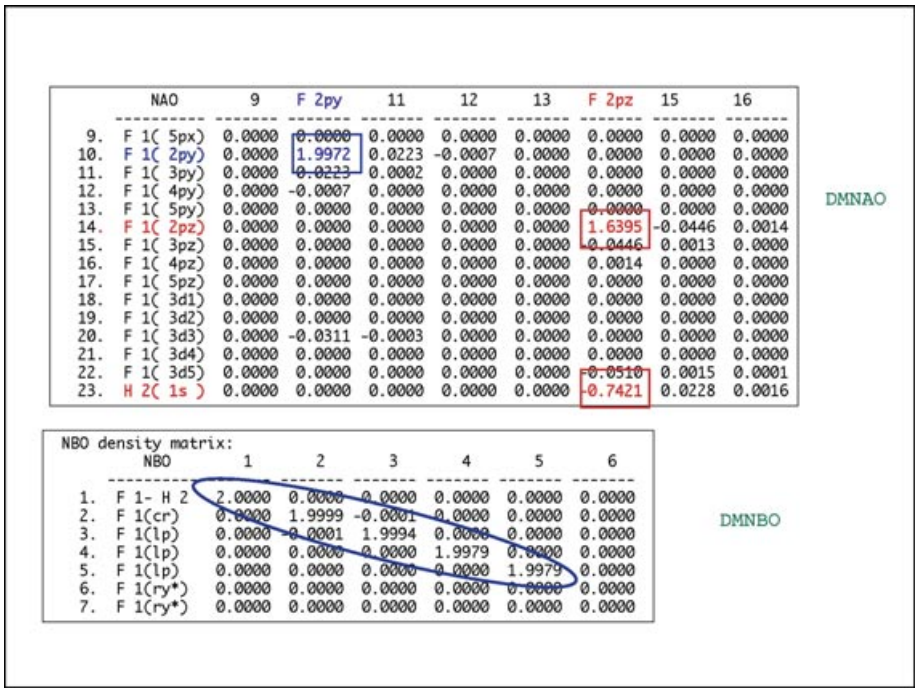


**FIGURE 9** | Density matrix in natural atomic orbital (NAO) (upper) and natural bond orbital (NBO) (lower) basis, showing high condensation of 'electron-pair' occupancy in diagonal DMNBO elements.

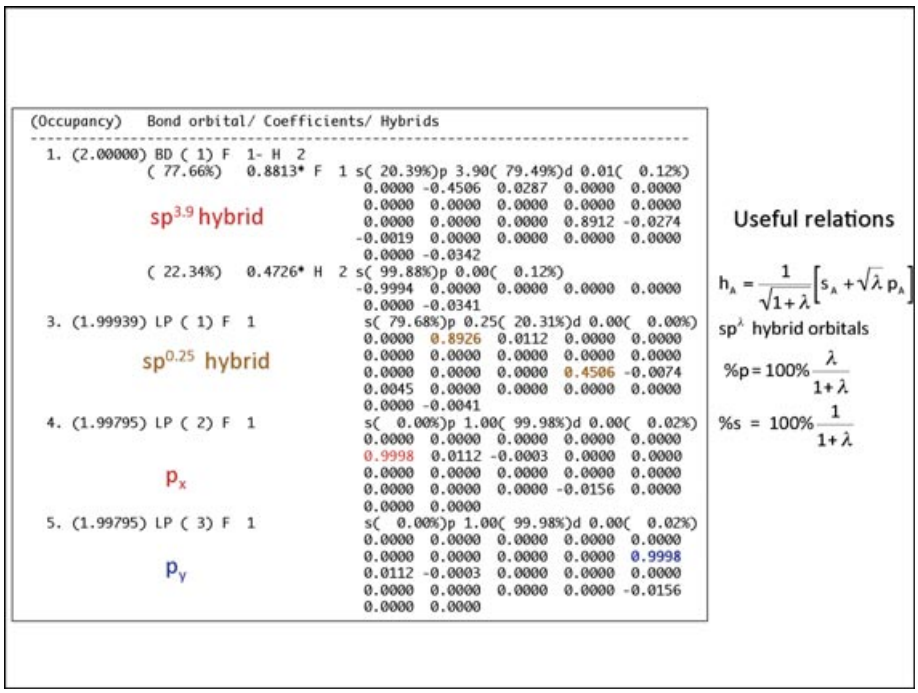


**FIGURE 10** | Natural bond orbital (NBO) listing with natural hybrid orbital (NHO) compositions and natural atomic orbital (NAO) coefficients, for hydrogen fluoride (HF) molecule.

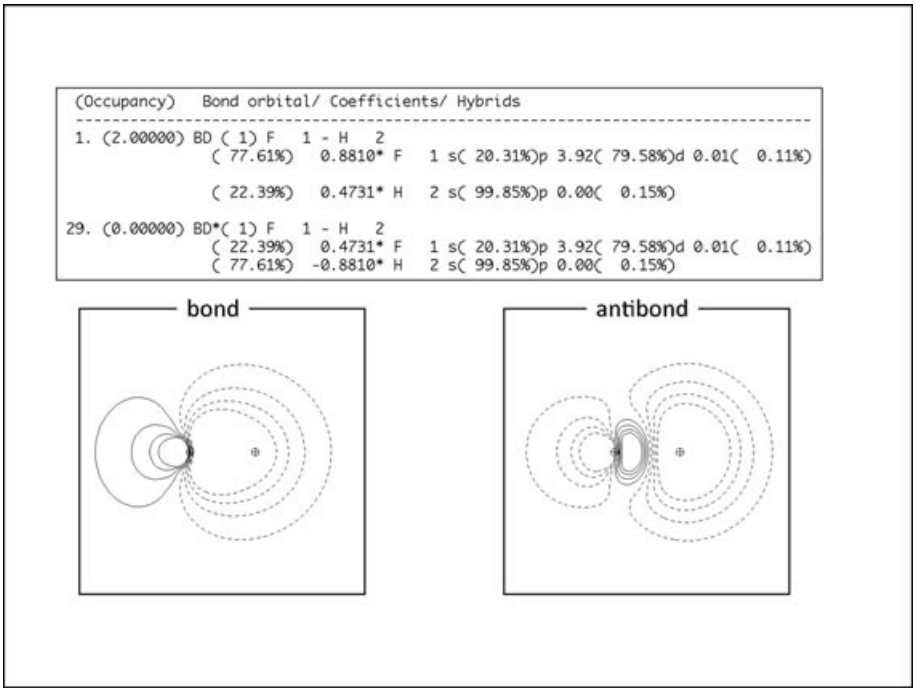


**FIGURE 11** | Comparison of valence-shell bond (NBO 1) and antibond (NBO 29) for hydrogen fluoride (HF) molecule.

includes contributions of polarization functions (d-type or other higher angular components of the chosen AO basis, typically negligible for valence hybrids), as explicitly displayed in the LCNAO-NBO coefficients for each hybrid, viz.,

$$h_F(sp^{3.90}) = 0.8912^*(2p_z)_F - 0.4506^*(2s)_F + \ldots. \quad (14d)$$

As seen from the squares of polarization coefficients $c_F$ and $c_H$, the $\sigma_{HF}$ NBO is primarily (77.66%) concentrated on F, consistent with its expected higher electronegativity. All these results are in highly satisfactory agreement with elementary Lewis/Pauling/Mulliken hybridization and bonding concepts, and all are broadly representative of what is to be expected in NBO analysis of molecules of arbitrary complexity.

It is noteworthy that the valence lone pairs, NBOs 3–5 (Figure 10), exhibit the physically required *in*equivalence between on-axis and off-axis orientation, rather than the 'tripod'-like equivalence suggested by valence-shell electron pair repulsions (VSEPR) concepts. On-axis LP(1) (NBO 3) differs from off-axis LP(2), LP(3) (NBOs 4, 5) in hybridization ($sp^{0.25}$ versus pure-p), occupancy (1.9994 versus 1.9980e) and other properties. Such inequivalence is physically and mathematically necessary because

- Hybridization (atomic s/p mixing and symmetry breaking) can only be driven by bonding interaction, and can only involve the $p_z$ orbital oriented along the bonding axis, whereas off-axis lone pairs retain pure $p_x$, $p_y$ angular character of the unperturbed atom;
- Dimensional conservation requires that on-axis s,$p_z$ orbitals in NAO space must reappear as oppositely directed p-rich ($sp^{3.90}$ bond hybrid) and s-rich ($sp^{0.25}$ lone pair hybrid) orbitals in NHO space.

In a similar vein, lone-pair hybridization in $H_2O$ can only involve the two in-plane ($p_x$, $p_y$) NAOs of the bonding framework, whereas the out-of-plane lone pair retains unhybridized pure-$p_z$ character, contrary to the VESEPR-inspired 'rabbit ears' picture. The quantitative forms of NHOs therefore provide a useful reality check on the illusory hybridization concepts fostered by VSEPR theory.

The leading high-occupancy L-type NBOs are typically followed by a long list of NL-type NBOs of negligible occupancy, particularly, extravalence RY* orbitals required for completeness in the chosen AO basis space. However, one such NL-type NBO, the $\sigma^*_{HF}$ 'antibond' (shown as BD*, NBO 29, in Figure 11), is of particular importance. It arises from the *same* valence NHOs that form $\sigma_{HF}$, but with *out*-of-phase mixing and *reversed* polarization coefficients

  

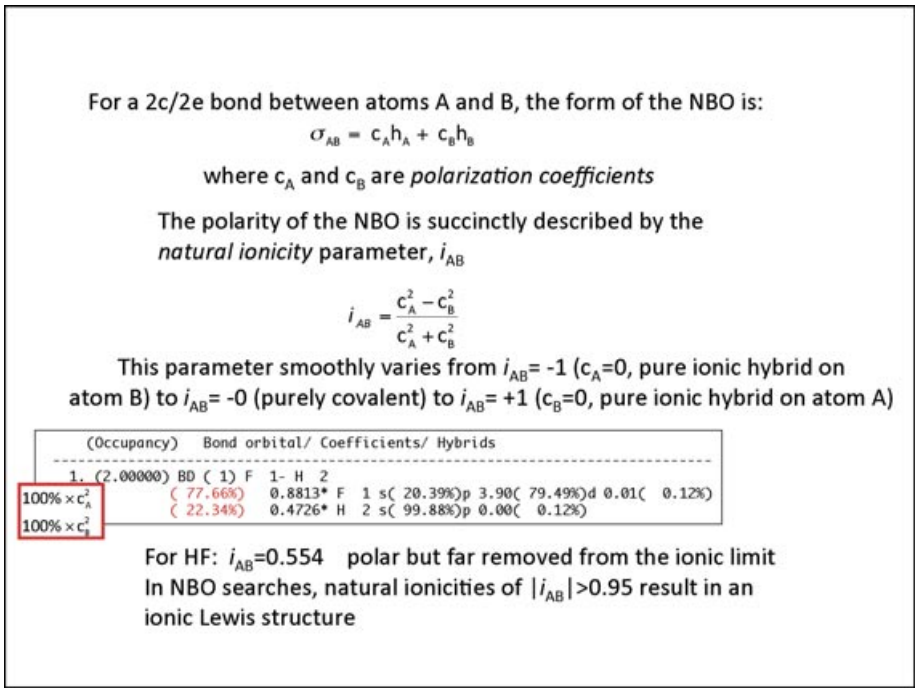


**FIGURE 12** | Details of hydrogen fluoride (HF) bond hybrid composition and ionicity.

to preserve orthonormality, viz.,

$$\sigma^*_{HF} = c_H h_F - c_F h_H = 0.4726^*(sp^{3.90})_F - 0.8813^*(s)_H. \quad (15)$$

[Recall that dimensional conservation in Hilbert space requires that two hybrids ($h_F$, $h_H$) in NHO space must be replaced by two orbitals ($\sigma_{HF}$, $\sigma^*_{HF}$) in NBO space.] Far from being 'anti' to bonding, this valence-shell NBO represents *residual valence-shell combining power*, the unused 'acceptor' capacity for additional bonding interactions with suitable L-type 'donor' orbitals of the intra- or intermolecular environment. However, as shown by its vanishing occupancy, such acceptor (Lewis acid) capacity remains unused in HF and other diatomics, so the importance of BD*-type NBOs only becomes apparent in more complex species. Nevertheless, we note from Figure 11 that the $\sigma^*_{HF}$ orbital is primarily concentrated toward H and exhibits most prominent angular 'bulging' beyond the H nucleus (consistent with its reversed polarity and the additional internuclear nodal phase change), suggesting the preferred angular orientation for successful interaction with an available donor orbital.

Figures 12 and 13 summarize how the $c_A$, $c_B$ polarization coefficiencts of a general $\sigma_{AB}$ bond NBO can be related to atomic electronegativities and the VB-theoretic covalent-ionic resonance mixing concept[25] through an NBO-based 'ionicity' descriptor of the form

$$i_{AB} = (c_A^2 - c_B^2)/(c_A^2 + c_B^2). \quad (16)$$

For HF, the calculated bond ionicity $i_{HF} = 0.554$ lies well below the value $|i_{AB}| > 0.95$ associated with classical ionic Lewis structures, showing the appreciable covalency of this molecular species. The bond ionicity parameter can also be correlated with s/p-character of bonding hybrids according to Bent's rule,[26] which draws a powerful connection between electronegativity differences and hybrid s/p-character (and accompanying bond angle variations), as summarized in Figure 13. Indeed, the expected correlation between ionicity ($i_{AH}$) and electronegativity differences ($\Xi_A - \Xi_H$) for elementary AH hydride bonds can be expressed as a mathematical relationship[27]

$$i_{AH} = 1 - \exp[-0.45(\Xi_A - \Xi_H)], \quad (17a)$$

which defines an NBO-based 'natural electronegativity' scale, viz.,

$$\Xi_A = \Xi_H - 2.22^*\ln(1 - i_{AH}) \quad (17b)$$

with intercept ($\Xi_H \equiv 2.10$) and slope fixed to express $\Xi_A$ in 'Pauling units'.[28] Figure 14 displays natural electronegativity values for the entire periodic table ($Z = 1 - 120$), obtained from calculated NBOs of normal-valent $AH_n$ hydrides at currently available theoretical levels.

  

Henry Bent formulated a remarkable rule correlating electronegativity with orbital hybridizations:

*A central atom tends to direct hybrids of higher p-character (greater λ) toward more electronegative substituents.*
or equivalently,
*Atomic s-character (lower λ) tends to accumulate in hybrids directed toward the least electronegative substituents*

Least electronegative substituent = vacuum => lone pairs tend to high s-character

Bent's rule suggests that
*electronegativities can be determined from NBO polarizations.*

Two useful equations: $i_{AH} = 1 - \exp[-0.45(\Xi_A - \Xi_H)]$

$$\Xi_A = \Xi_H - \frac{\ln(1 - i_{AH})}{0.45}$$

For HF, $\Xi_F - \Xi_H$ = -ln(1-0.556)/0.45=1.80
(Pauling $\Xi_F - \Xi_H$=3.98-2.2=1.78)

**FIGURE 13** | Summary of Bent's rule and natural bond orbital (NBO) based relationship of electronegativity and bond polarity.

| Z | atom | $\Xi_A^{(e)}$ | Z | atom | $\Xi_A^{(e)}$ | Z | atom | $\Xi_A^{(e)}$ | Z | atom | $\Xi_A^{(e)}$ |
|---|---|---|---|---|---|---|---|---|---|---|---|
| 1 | H | [2.10] | 31 | Ga | 1.39 | 61 | Pm | (0.96) | 91 | Pa | (1.06) |
| 2 | He | (4.04) | 32 | Ge | 1.74 | 62 | Te | (0.97) | 92 | U | (0.99) |
| 3 | Li | 0.79 | 33 | As | 1.93 | 63 | Eu | (0.80) | 93 | Np | (1.15) |
| 4 | Be | 1.02 | 34 | Se | 2.21 | 64 | Gd | (0.96) | 94 | Pu | (1.07) |
| 5 | B | 1.86 | 35 | Br | 2.47 | 65 | Tb | (0.96) | 95 | Am | (0.90) |
| 6 | C | 2.60 | 36 | Kr | (2.73) | 66 | Dy | (0.97) | 96 | Cm | (1.04) |
| 7 | N | 3.07 | 37 | Rb | 0.83 | 67 | Ho | (0.93) | 97 | Bk | (1.04) |
| 8 | O | 3.48 | 38 | Sr | 0.83 | 68 | Er | (0.81) | 98 | Cf | (1.04) |
| 9 | F | 3.89 | 39 | Y | 1.09 | 69 | Tm | (0.79) | 99 | Es | (0.98) |
| 10 | Ne | (4.44) | 40 | Zr | 1.43 | 70 | Yb | (0.82) | 100 | Fm | (0.85) |
| 11 | Na | 0.88 | 41 | Nb | 1.67 | 71 | Lu | (1.01) | 101 | Md | (1.10) |
| 12 | Mg | 1.04 | 42 | Mo | 2.16 | 72 | Hf | 1.34 | 102 | No | (0.96) |
| 13 | Al | 1.35 | 43 | Tc | 2.25 | 73 | Ta | 1.54 | 103 | Lr | (1.00) |
| 14 | Si | 1.78 | 44 | Ru | 2.31 | 74 | W | 1.94 | 104 | Rf | (1.25) |
| 15 | P | 2.06 | 45 | Rh | 2.23 | 75 | Re | 2.20 | 105 | Db | (1.42) |
| 16 | S | 2.42 | 46 | Pd | 2.04 | 76 | Os | 2.17 | 106 | Sg | (1.72) |
| 17 | Cl | 2.76 | 47 | Ag | 1.48 | 77 | Ir | 2.22 | 107 | Bh | (2.15) |
| 18 | Ar | (3.12) | 48 | Cd | (1.18) | 78 | Pt | 2.30 | 108 | Hs | (2.10) |
| 19 | K | 0.82 | 49 | In | 1.32 | 79 | Au | 2.01 | 109 | Mt | (2.21) |
| 20 | Ca | 0.87 | 50 | Sc | 1.58 | 80 | Hg | (1.51) | 110 | Ds | (2.40) |
| 21 | Sc | 1.16 | 51 | Sb | 1.72 | 81 | Tl | 1.43 | 111 | Rg | (2.26) |
| 22 | Ti | 1.55 | 52 | Te | 1.95 | 82 | Pb | 1.64 | 112 | Uub | (1.84) |
| 23 | V | 1.79 | 53 | I | 2.19 | 83 | Bi | 1.70 | 113 | Uut | (1.48) |
| 24 | Cr | (1.16) | 54 | Xe | (2.40) | 84 | Po | (1.92) | 114 | Uuq | (1.60) |
| 25 | Mn | (2.03) | 55 | Cs | 0.81 | 85 | At | (2.16) | 115 | Uup | (1.68) |
| 26 | Fe | 2.03 | 56 | Ba | 0.78 | 86 | Rn | (2.28) | 116 | Uuh | (1.88) |
| 27 | Co | 1.96 | 57 | La | (0.88) | 87 | Fr | (0.74) | 117 | Uus | (2.12) |
| 28 | Ni | 1.87 | 58 | Ce | (0.82) | 88 | Ra | (0.81) | 118 | Uuo | (2.20) |
| 29 | Cu | 1.47 | 59 | Pr | (0.80) | 89 | Ac | (0.79) | 119 | ? | (0.67) |
| 30 | Zn | (1.17) | 60 | Nd | (0.93) | 90 | Th | (0.95) | 120 | ? | (0.79) |

**FIGURE 14** | Table of natural electronegativity values for elements 1–120, as calculated from natural bond orbital (NBO) polarities of ground-state $AH_n$ Lewis-like hydrides.

Figure 15 displays amplitude profiles of the $2s_F$, $2p_F$ NAOs of HF (left panels), comparing their forms with corresponding 'pre-NAOs' (PNAOs) in which interatomic orthogonalization ('steric pressure') has been ignored. The PNAOs may be thought of as free-atom-like *visualization* orbitals that match the true (orthonormal) NAOs as closely as possible, but include nonvanishing overlap contributions (neglected

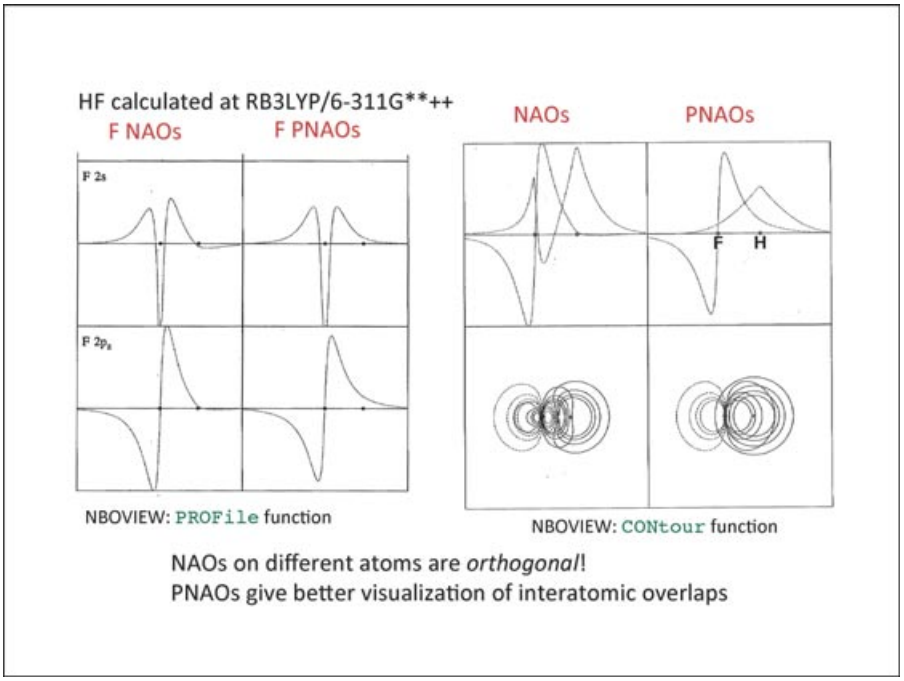


**FIGURE 15** | Comparison of orthogonal natural atomic orbitals (NAOs) and overlapping PNAOs ('visualization orbitals') for hydrogen fluoride (HF) molecule.

interatomic nodal features) that permit useful 'eyeball estimates' of physical $\langle \mathrm{NHO}_i|\mathbf{F}|\mathrm{NHO}_j\rangle$ interaction strength through Mulliken or Wolfsberg–Helmholz approximations of the form[29–31]

$$\langle \mathrm{NAO}_i|\mathbf{F}|\mathrm{NAO}_j\rangle \cong -k\langle \mathrm{PNAO}_i|\mathrm{PNAO}_j\rangle = -kS_{i,j}, \tag{18}$$

where $k$ is a constant of order unity. The PNAOs thereby allow one to retain the benefits of 'maximum overlap' conceptual reasoning, while avoiding insidious effects of overlap contamination in pseudoperturbative equations. The combined usage of NAOs versus PNAOs (as well as corresponding NHOs vs. PNHOs, or NBOs vs. PNBOs, etc.) for complementary computation versus visualization purposes is one of the most characteristic and powerful features of NBO-based methods. Unless otherwise stated, NBO-based orbital diagrams (as obtained, e.g., with the NBOView 1.0 orbital viewer program[32]) are usually displaying preorthogonal PNAOs, PNHOs, or PNBOs (rather than orthogonal NAOs, NHOs, and NBOs) to exploit the pedagogical advantages of these visualization orbitals.

The four panels at the left of Figure 15 show that NAOs of the F atom appear 'scrunched up' compared to free-atom PNAOs on the side toward H, reflecting the breaking of atomic rotational symmetry in the molecular environment. The four panels at the right show both $(2p)_F$ and $(1s)_H$ NAOs and PNAOs of HF in profile (upper) and contour (lower) views. As seen in the upper-right panel, the facing lobes of $(2p)_F$ and $(1s)_H$ PNAOs 'pass through' (overlap) one another, unrealistically oblivious to the steric pressure of electron density on the adjacent atom. In contrast, NAOs remain mutually orthogonal (as physical orbitals must!) to incorporate the important physical effects of steric exchange repulsion at all separations.

Similar remarks apply to directed hybrid NHOs versus overlapping PNHOs, where the latter have identical s/p mixing coefficients but are built from PNAOs rather than NAOs. Figure 16 displays further details of $\sigma_{\mathrm{HF}}$ NBO formation in terms of complementary PNHO versus NHO representations. Despite what beginning students are sometimes taught, nonoverlapping hybrids *can and do* lead to interaction, as numerically demonstrated for the NHOs of HF in Figure 17.

Figure 18 displays the natural atomic charges ($q_F = -q_H = -0.548$) and other 'natural electron configuration' (NEC) details of this polar molecule. For simple diatomic species such as HF, one finds the expected relationship $q_F \cong i_{HF}$ between atomic charge and bond ionicity. Such cross-checks illustrate the self-consistency of 'charge budget' and other electronic properties that must extend to all aspects of NAO/NHO/NBO description.

  

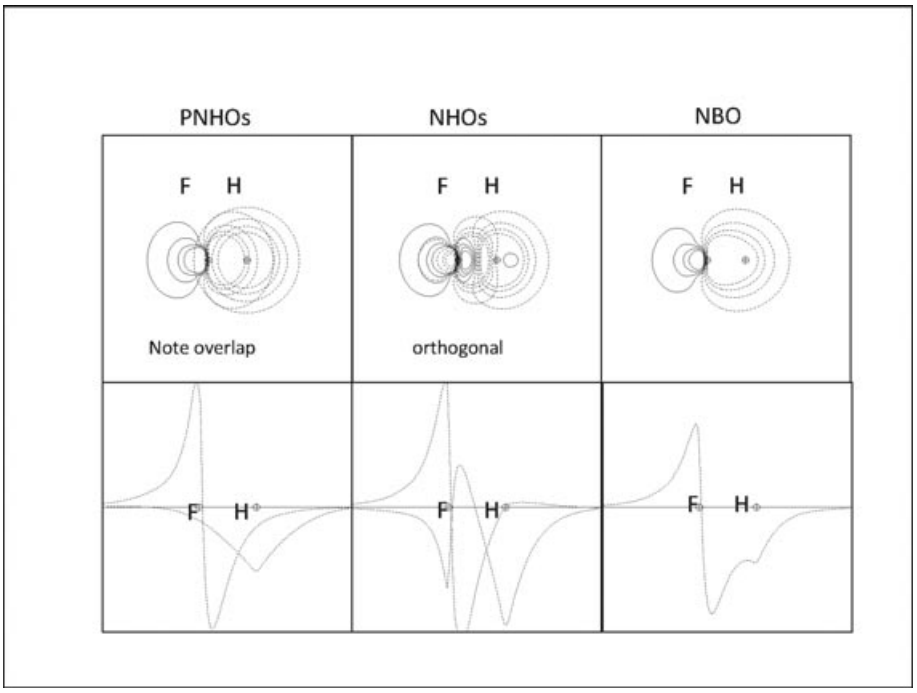


**FIGURE 16** | Natural hybrid orbital (NHO) (orthogonal) versus PNHO (nonorthogonal) comparisons for hydrogen fluoride (HF) molecule.

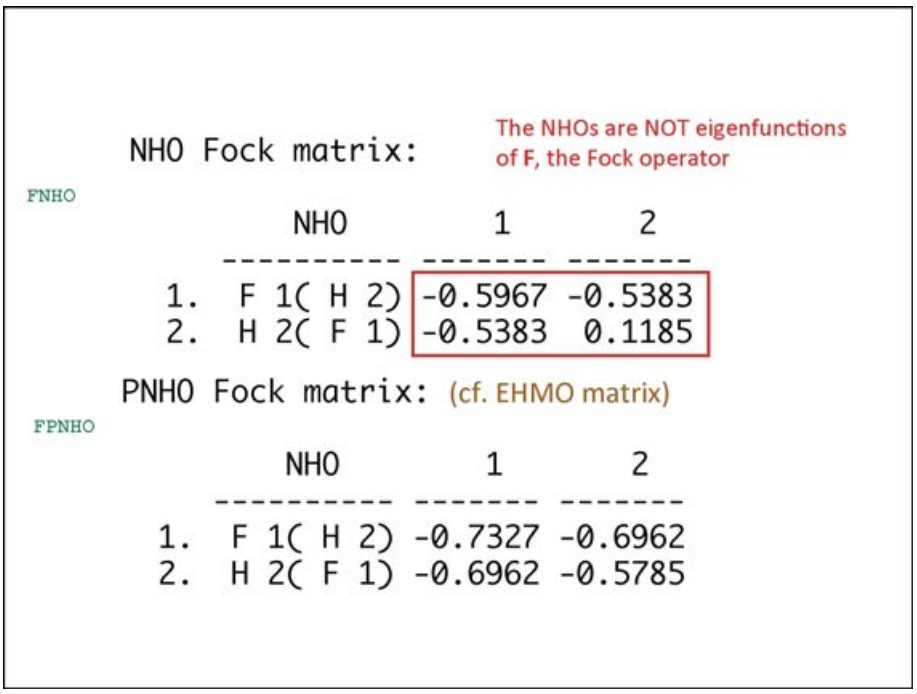


**FIGURE 17** | Natural hybrid orbital (NHO) Fock matrix for hydrogen fluoride (HF), showing strong off-diagonal interaction element between NHOs despite their mutual orthogonality.

Let us finally consider the somewhat more complex NBO description in an open-shell diatomic species such as $O_2$. In this case, the expected DODS character of $\alpha$ and $\beta$ spin distributions leads to corresponding 'different Lewis structures for different spins' (DLDS) character for $\alpha$- and $\beta$-NBOs. The distinct NLS dot diagrams for $\alpha$ and $\beta$ spins of triplet $O_2$ are shown in Figure 19, corresponding to distinct

  

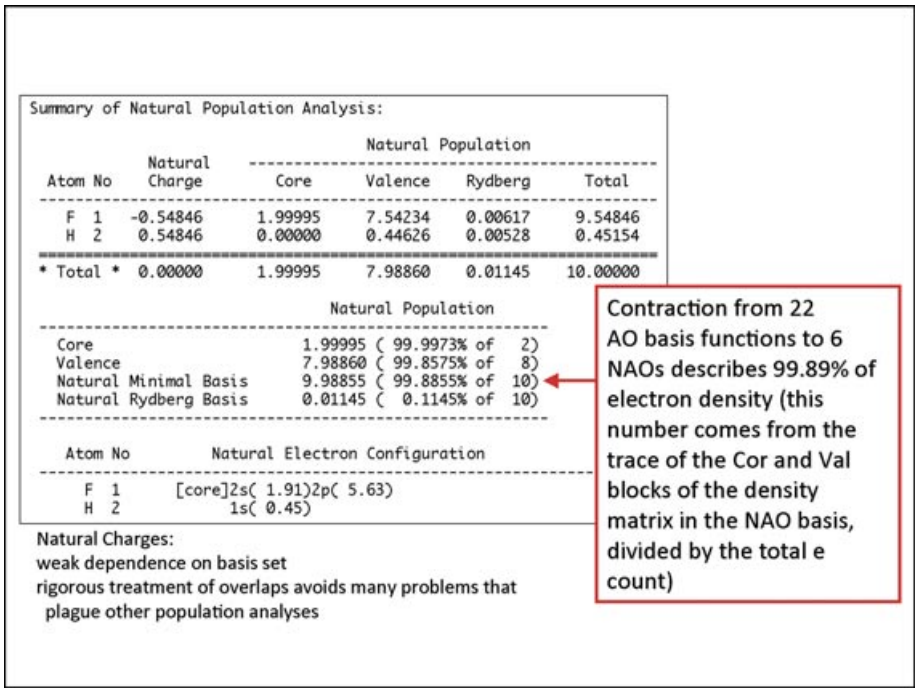


**FIGURE 18** | Natural population analysis (NPA) summary output for hydrogen fluoride (HF), showing effective condensation of electron occupancy (99.9%) in the 'natural minimal basis' set of natural atomic orbitals (NAOs).

single ($\alpha$) and triple ($\beta$) (half-)bonded structures in the two spin sets. The overall properties of the $^3O_2$ species can therefore be pictured as the spin-averaged composite ('spin hybrid') of distinct $\alpha$-NLS and $\beta$-NLS representations, with, e.g., composite bond order 1/2 + 3/2 = 2. The on-axis LP (nonbonding 'lone particle') NBOs are also seen to be of distinct form in the two spin sets (viz., $sp^{0.22}$ for $\alpha$ spin, $sp^{0.26}$ for $\beta$ spin), showing how nonvanishing spin density can also extend into NBOs that are nominally 'doubly occupied'. With the simple DLDS generalization, the accuracy of NBO description of open-shell species generally rivals that of closed-shell species.

DLDS splitting of open-shell NBO bonding patterns reminds us that the essential feature of Lewis-structural description is the localized 1c/2c character of occupied spin-orbitals, rather than 'pairing' *per se*. Exact RHF-type 'double occupancy' should therefore be recognized as a special case of Lewis-like bonding that is often achieved by familiar singlet species in ground-state near-equilibrium geometry (ozone being a notable exception), but is only a highly *im*plausible idealization for other geometries, states of excitation, or spin multiplicities. The general DLDS viewpoint also underlies description of covalent bond formation as the limiting result of *two distinct 1e donor–acceptor interactions of opposite spin* that evolve from radical reactant species at long range toward final closed-shell (spin-paired) product species at shorter range.[33]

## Polyatomics

Passing beyond diatomics to general polyatomic species allows us to see the full beauty and power of localized NBO methods. Before examining specific species, we discuss general aspects of hybrid orientation, molecular geometry, and inter-bond coupling effects ('conjugative' or 'resonance-type' donor–acceptor interactions) that pertain to the polyatomic domain.

Figure 20 summarizes the basic hybridization equations that lead to *Coulson's directionality theorem* for the idealized bond angle $\omega_{AB}$ between directed $sp^{\lambda}$ hybrids of distinct $\lambda_A$, $\lambda_B$ character emanating from a common center, viz.,

$$\cos(\omega_{AB}) = -(\lambda_A\lambda_B)^{-1/2}. \qquad (19)$$

For equivalent $sp^3$ hybrids ($\lambda_A = \lambda_B = 3$), Eq. (19) leads to the familiar tetrahedral bond angle, $\omega_{AB} = \cos^{-1}(-1/3) = 109.47^\circ$, and similarly for other equivalent $sp^2$ or $sp^1$ hybrids. However, the formula also describes idealized bond angles for *in*equivalent hybrids as required by Bent's rule (Figure 13), thereby providing a deeper rationalization for geometry

  

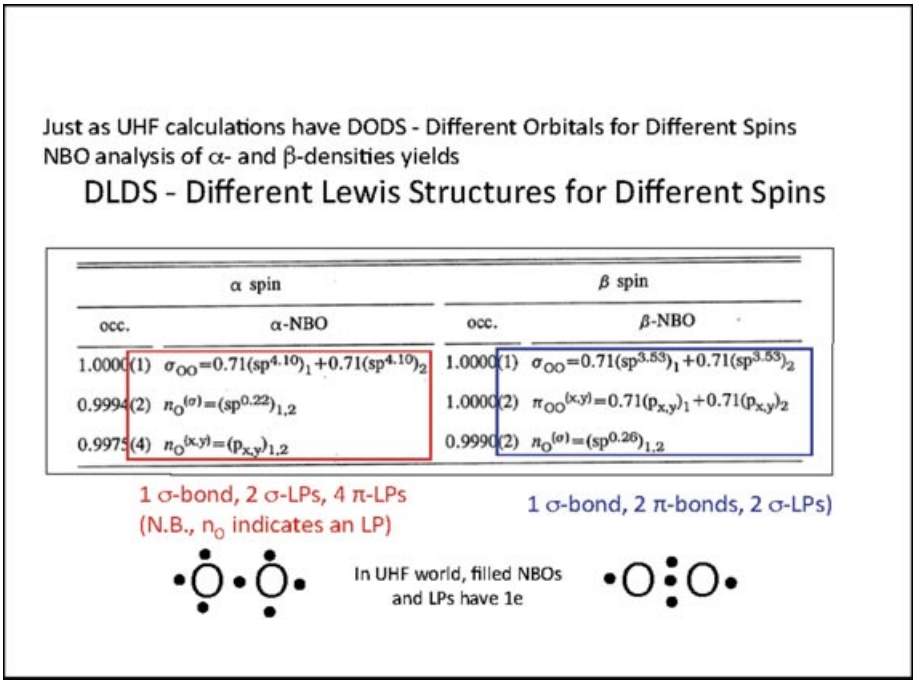


**FIGURE 19** | Comparison of alpha and beta spin natural bond orbitals (NBOs) for $O_2$, showing 'different Lewis structures for different spins' open-shell character.

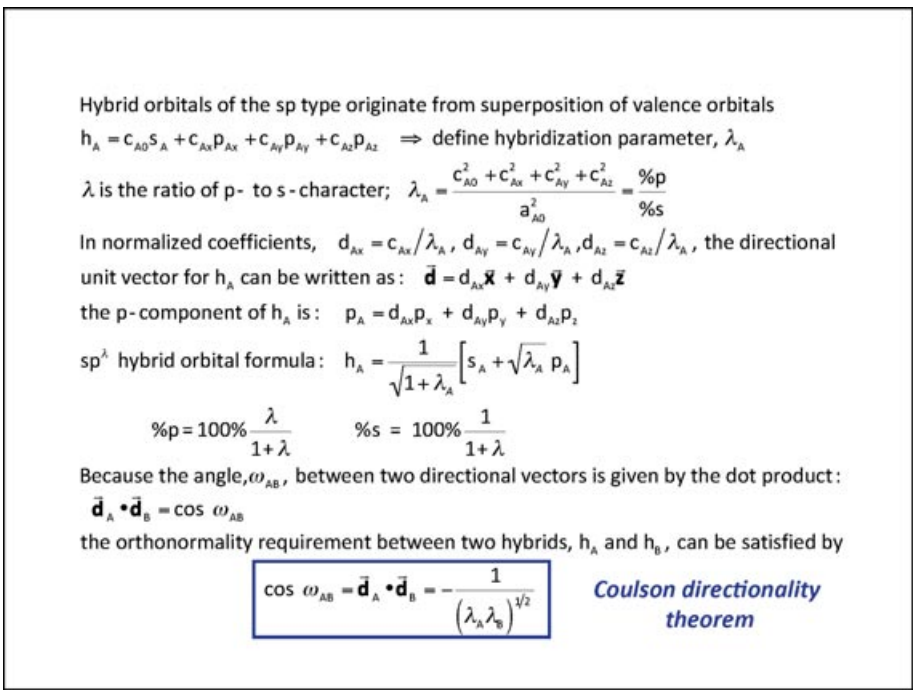


**FIGURE 20** | Hybrid composition versus hybrid directionality relationship as summarized in Coulson's theorem.

variations that are often explained superficially by VSEPR theory.

Recognition of the principal donor (L-type) and acceptor (NL-type) NBOs leads to the formal perturbation theory of NBO donor–acceptor interactions[34] as summarized in Figure 21. As shown in the diagram, interaction of unperturbed donor $\varphi_i^{(0)}$ (e.g., a valence lone pair) with acceptor $\varphi_{j*}^{(0)}$ (e.g., a valence

  

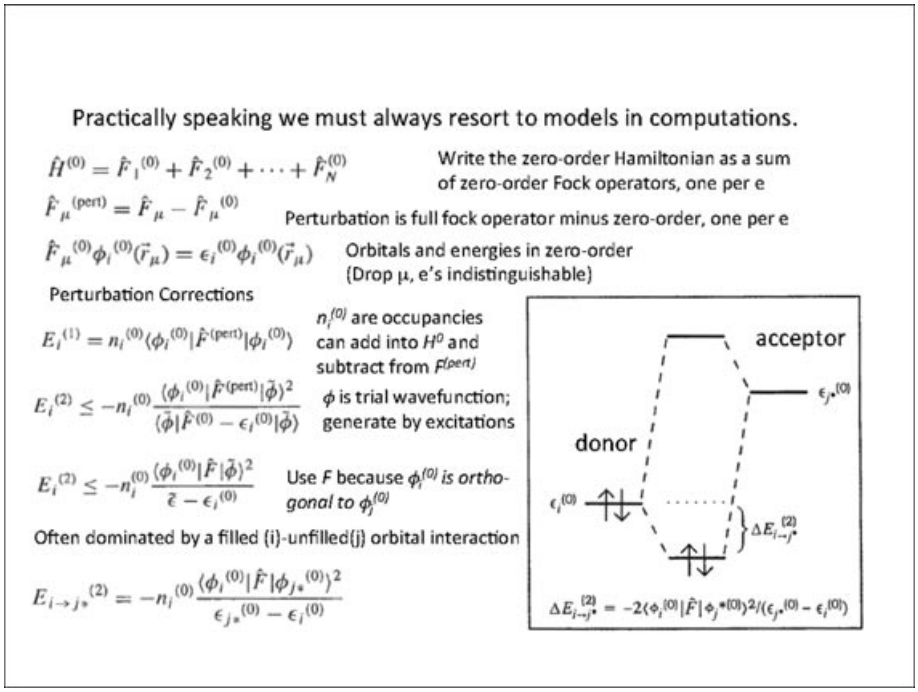


**FIGURE 21** | Mathematical and graphical summary of natural bond orbital (NBO) donor–acceptor perturbation theory.

antibond) leads to the corresponding second-order $i \to j^*$ stabilization estimate

$$\Delta E^{(2)}_{i\to j^*} = -2\langle\varphi_i^{(0)}|\mathbf{F}|\varphi_{j^*}^{(0)}\rangle^2 \big/ \left(\varepsilon_{j^*}^{(0)} - \varepsilon_i^{(0)}\right). \quad (20)$$

The donor–acceptor diagram depicts a universal quantum mechanical paradigm[35] for energetically stabilizing ('rewarding') the superposition of occupied and unoccupied localized orbitals in chemical-type interactions such as

- *chemical bonding* (e.g., occupied $s_A$ NAO on atom A with unoccupied $s^*_B$ NAO on atom B);
- *polyatomic conjugation* (e.g., occupied $\pi_{AB}$-bond NBO with unoccupied $\pi_{CD}{}^*$-antibond NBO in vicinal A = B − C = D connectivity);
- *supramolecular aggregation* (e.g., occupied $n_B$ lone pair on molecule B: with unoccupied $\sigma^*_{AH}$ antibond NBO on hydride molecule HA in B:···HA alignment).

Note the *squared* dependence on **F** in (20), which insures that the intrinsic energy-*lowering* of donor–acceptor interactions is essentially independent of many details of the system Hamiltonian.

The perturbation-theoretic equations of Figure 21 are formulated in terms of a rather generic decomposition into 'unperturbed' (0) and 'perturbation' (pert) components, e.g., for the 1e Hartree–Fock or Kohn–Sham Hamiltonian,

$$\mathbf{F} = \mathbf{F}^{(0)} + \mathbf{F}^{(\text{pert})}. \quad (21)$$

Each such splitting into $\mathbf{F}^{(0)}$ and $\mathbf{F}^{(\text{pert})}$ $(= \mathbf{F} - \mathbf{F}^{(0)})$ provides an alternative 'perturbative model' for describing the complex final **F** in terms of a starting unperturbed $\mathbf{F}^{(0)}$ that is 'easier to understand'. As in Eqs (2) and (3), we can employ the NBO basis to construct a Lewis-like $\mathbf{F}^{(L)}$ to serve as the starting point for perturbative 'resonance' corrections. In such constructions, it becomes apparent that *better basis sets give better perturbative models*, and NAO/NBO-based models are virtually *defined* to guarantee optimal Lewis-like description of bonding interactions.

The high accuracy of NAO/NBO-based perturbative methods rests on the accuracy of the Lewis model itself. The highly occupied L-type NBOs $\{\Omega_i^{(L)}\}$ ($N/2$ in number) define the idealized NLS wavefunction:

$$\Psi^{(L)}(1, 2, \ldots, N) = (N!)^{-1/2}\det|(\Omega_1)^2(\Omega_1)^2\ldots(\Omega_{N/2})^2|; \quad (22a)$$

'Lewis density' $\rho^{(L)}$:

$$\rho^{(L)} = \sum_i n_i \left|\Omega_i^{(L)}\right|^2 (i = 1, 2, \ldots. N/2); \quad (22b)$$

and energy $E^{(L)}$ of idealized NLS description:

$$E^{(L)} = \int \psi^{(L)^*}\mathbf{H}\psi^{(L)}d\tau. \quad (22c)$$

The remaining NL-type NBOs $\{\Omega_i^{(L)}\}$ complete the span of the basis,

$$\{\Omega_i\} = \{\Omega_i^{(L)}\} + \{\Omega_j^{(NL)}\}, \quad (23a)$$

allowing one to similarly decompose the total wavefunction, electron density, and energy into L/NL components, viz.,

$$\Psi = \Psi(L) + \Psi(NL), \quad (23b)$$

$$\rho = \rho^{(L)} + \rho^{(NL)}, \quad (23c)$$

$$E = E^{(L)} + E^{(NL)}. \quad (23d)$$

For common chemical species ($H_2O$, $CH_4$,...) the L-type contribution is extraordinarily dominant (~99.9%), insuring rapid perturbative convergence for NL-type corrections.

In HF/DFT framework, one begins by constructing the formal L-type Fock operator $\mathbf{F}^{(L)}$ for which

$$\mathbf{F}^{(L)}\Omega_i^{(L)} = \varepsilon_i^{(L)}\Omega_i^{(L)} \quad (24)$$

and *resonance effects are absent*. (A formal *Ne* Hamiltonian $\mathbf{H}^{(L)}$ is similarly constructed as the sum of such 1e $\mathbf{F}^{(L)}$ operators.) The resonance-free world of $\mathbf{F}^{(L)}$ is thereby divided into noninteracting donor (L) and acceptor (NL) domains, viz.,

$$\text{Donors } \{\Omega_i^{(L)}\} : \sigma_{AB},\ \sigma_{BC},\ n_A,\ \text{etc.}, \quad (25a)$$

$$\text{Acceptors } \{\Omega_j^{(NL)}\} : \sigma^*_{AB}, \sigma^*_{CD}, r_A, \text{etc.}, \quad (25b)$$

in which

$$\langle\Omega_i^{(L)}|\mathbf{F}^{(L)}|\Omega_j^{(NL)}\rangle = 0 \text{ for all } i,\ j. \quad (26)$$

However, in the real world of the full Fock/Kohn–Sham **F** operator, such donor–acceptor interactions (variously called 'charge transfer', 'delocalization', or 'resonance' effects) are generally nonvanishing

$$F_{ij}^{(NBO)} = \langle\Omega_i^{(L)}|\mathbf{F}|\Omega_j^{(NL)}\rangle \neq 0, \quad (27)$$

leading to the stabilizations depicted in Eq. (20) and Figure 21. As usual [cf. Eq. (18)], the numerical $F_{ij}^{(NBO)}$ matrix elements can be effectively 'guesstimated' in terms of the overlap $S_{ij}^{(PNAO)}$ of corresponding preorthogonal PNBO orbitals, viz.,

$$F_{ij}^{(NBO)} \cong -kS_{ij}^{(PNBO)}, \quad (28)$$

thereby providing powerful visual imagery of the strength of donor–acceptor interactions.

Let us examine a species for which errors of the idealized L-type description are unusually large. For this purpose we choose the interesting case of formamide ($NH_2CHO$), which leads to the NBO output displayed in Figure 22 (B3LYP/6–311++G** level). As shown in the NBO search summary, despite investigation of many possible bonding patterns (with different numbers and locations of BD and LP NBOs, different occupancy thresholds, etc.), the best NLS still harbors non-Lewis 'errors' of ~0.46e, about 2.5% of valence density (or 1.9% of total density). What's going on here?

Figure 23 shows NBO Summary details for the leading Lewis structure (with N–C=O amide bond pattern). Even though hybridization and polarization details of the NBOs have been skipped over in this output snippet (cf. Figures 10 and 19), one can recognize that 'BD(1)' ($\pi_{CO}$, NBO 4) and 'BD(2)' ($\sigma_{CO}$, NBO 5) of the C=O double bond are *in*equivalent ($\sigma/\pi$ rather than 'banana bonds'), as are also the 'LP(1)' (NBO 11, $n_O^{(s)}$) and 'LP(2)' (NBO 12, $n_O^{(p)}$) lone pairs of the carbonyl oxygen (no 'rabbit ears'!). As highlighted in the upper box, the greatest deviation of L-type NBOs from idealized Lewis-structural form appears at the $n_N$ lone pair on N, whose occupancy (1.748e) differs markedly from the expected 'electron pair'. Most of this 'missing' occupancy (0.246e) is found in the $\pi^*_{CO}$ NBO ['BD*(1)', NBO 88], indicating that some kind of $n_N \rightarrow \pi^*_{CO}$ 'charge transfer' is going on (as discussed below).

Even in the absence of an NBO orbital viewer (e.g., Ref 32), one can infer some features of NBO shape and orientation from the 'NHO Directionality and Bond Bending' table that follows NBO Summary output (Figure 24). This table shows the orientation of bonding NHOs in the polar coordinates ($\theta$, $\varphi$) of the host electronic structure system (ESS). Most useful are the deviation ('Dev') angles from the direct line of nuclear centers. For NHOs in sigma-bonding orientation, the DEV values are ~0 (with $\sigma_{CH}$, NBO 6, showing slightly greater 'bond-bending' in this relatively unstrained case), whereas perpendicular pi-type orientation corresponds to DEV = ~90. All the results are in close correspondence with the freshman chemistry picture of $H_2NCH{=}O$ hybridization and bonding.

Given the large NL occupancies of Figure 23, one can anticipate that NBO donor–acceptor interactions are of particular importance in formamide. Figure 25 displays calculated second-order 'E(2)' estimates of donor–acceptor interaction strength [note the sign reversal with respect to Eq. (20)], showing the dominant stabilization (~59.6 kcal/mol) due to $n_N \rightarrow \pi^*_{CO}$ (NBOs 10 → 85) charge transfer, as anticipated above. [The final two columns exhibit the NBO orbital energy difference 'E(*j*)–E(*i*)' and Fock

  

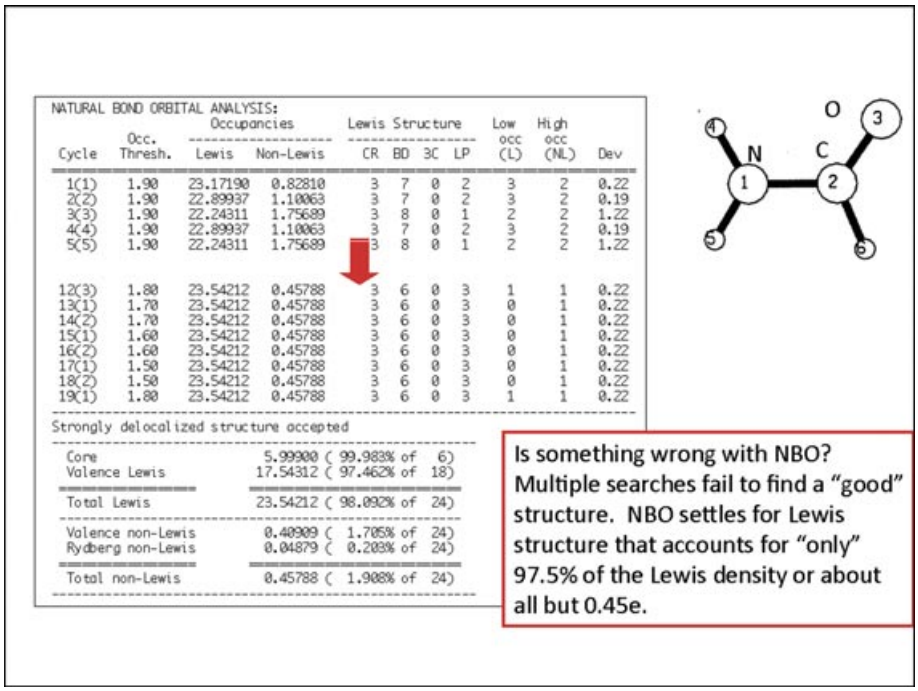


**FIGURE 22** | Natural bond orbital (NBO) search summary for formamide ($NH_2CHO$), showing unusually large non-Lewis 'errors' associated with quantum mechanical resonance.

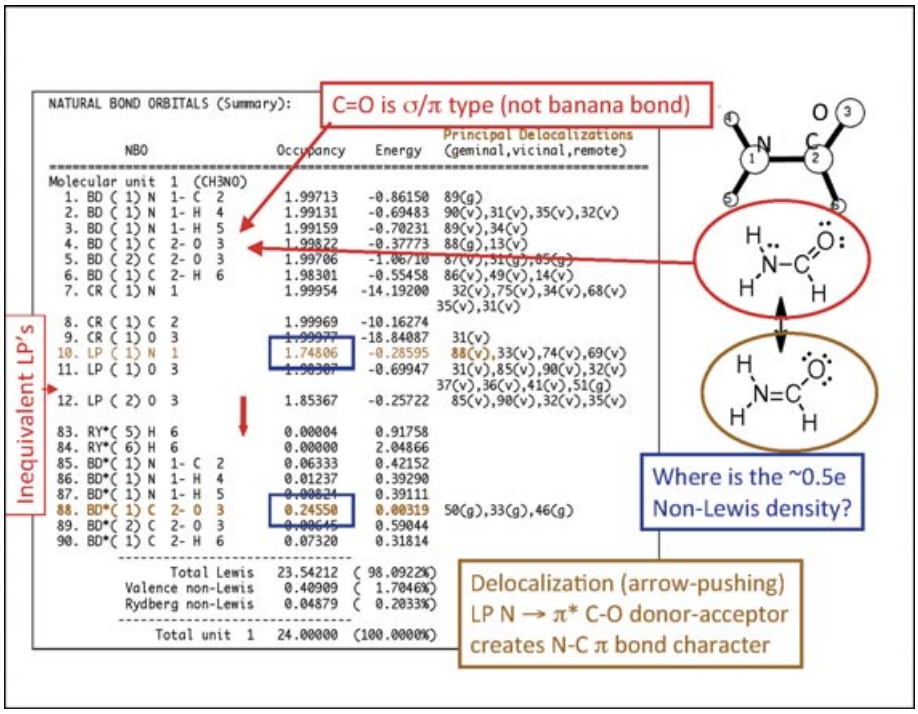


**FIGURE 23** | Natural bond orbital (NBO) summary output for formamide, showing the evident 'charge transfer' from $n_N$ lone pair (NBO 10) to $\pi_{CO}^*$ antibond (NBO 88) that underlies amide resonance.

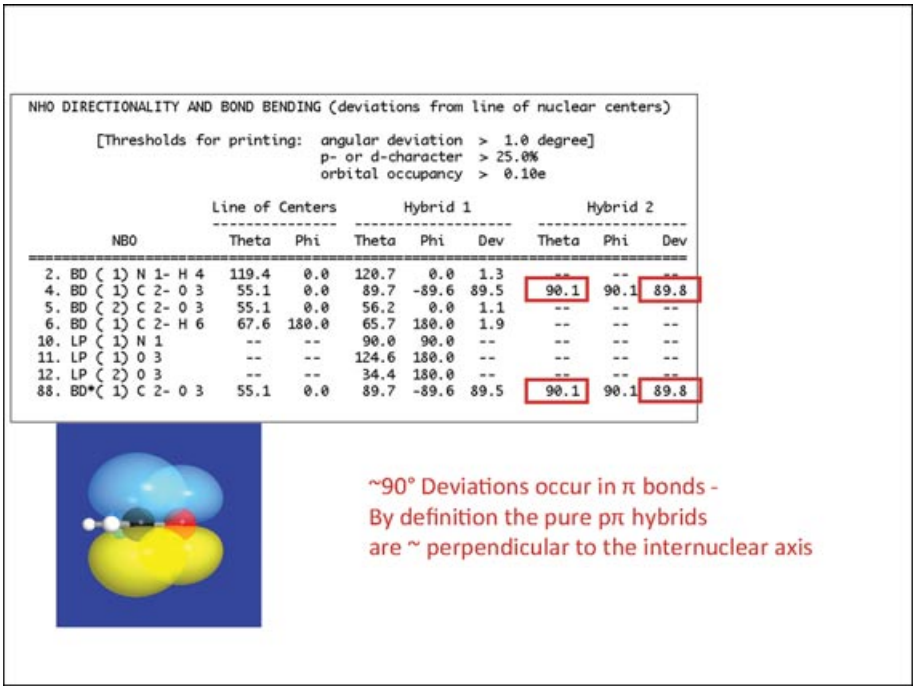


**FIGURE 24** | Natural hybrid orbital (NHO) directionality output for formamide, showing 'bond bending' descriptors for sigma and pi bonds.

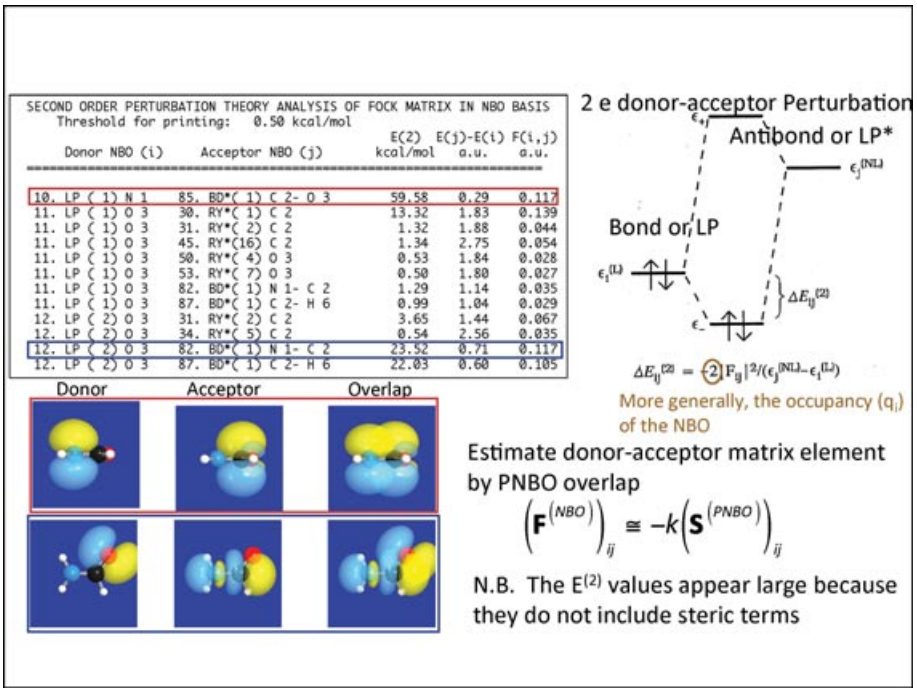


**FIGURE 25** | Natural bond orbital (NBO) second-order perturbation theory output for 'E(2)' donor–acceptor interactions of formamide, showing dominant stabilization (~60 kcal/mol) due to $n_N \rightarrow \pi_{CO}^*$ delocalization, as pictured in PNBO overlap diagrams [cf. Figure 21 for mathematical details of tabulated 'E(*j*) − E(*i*)' orbital energy differences and 'F(*i*, *j*)' Fock matrix elements].

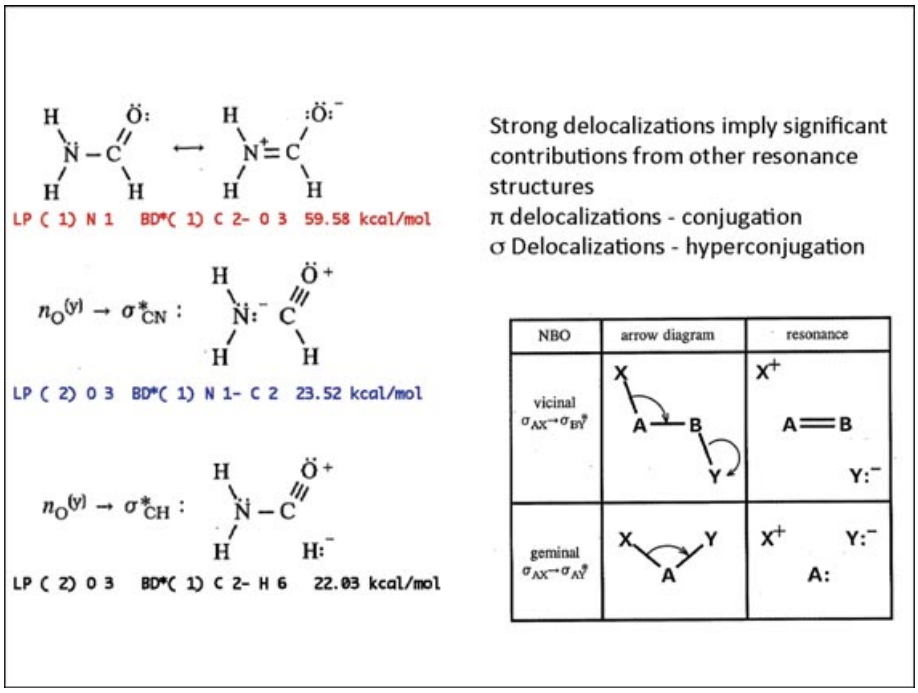


**FIGURE 26** | Mnemonic table relating natural bond orbital (NBO) donor–acceptor interactions to associated 'arrow pushing' and resonance diagrams, with details of leading interactions and resonance structures for formamide.

matrix element 'F(*i*,*j*)' needed to evaluate E(2) from Eq. (20).] The NBOView panels below display orbital imagery for the leading two delocalizations, $n_N \rightarrow \pi^*_{CO}$ (upper) and $n_O{}^{(p)} \rightarrow \sigma_{CN}$ (lower), showing the favorable (P)NBO donor–acceptor overlap in each case. Mulliken-type comparisons (20) allow one to visually recognize why, e.g., $n_O{}^{(p)} \rightarrow \sigma^*_{CN}$ (12 → 82; 23.5 kcal/mol) is vastly more important than $n_O{}^{(s)} \rightarrow \sigma^*_{CN}$ (11 → 82; 1.3 kcal/mol) as a secondary 'hyperconjugative' stabilization.

The expected mnemonic relationship between NBO donor–acceptor E(2) values and traditional organic resonance and 'arrow pushing' concepts is displayed in the lower-right panel of Figure 26. Each NBO donor–acceptor delocalization can be associated with a configurational reassignment corresponding to admixture of the alternative resonance structure (see, e.g., Ref 6, pp. 20, 263), thus 'translating' NBO donor–acceptor concepts into the language of resonance theory. As described below, calculated NBO E(2) values are expected to correlate with resonance weights inferred for these structures on empirical grounds.

As the second-order perturbation diagram (Figure 21) suggests, the mixing of donor $\Omega_i^{(L)}$ and acceptor $\Omega_j^{(NL)}$ NBOs leads to final *semi*localized orbitals $\Phi_i^{(L)}$, $\Phi_j^{(NL)}$ that can be expressed as

$$\Phi_i^{(L)} = (1 - t_{ij}^2)^{1/2}\,\Omega_i^{(L)} + t_{ij}\Omega_j^{(NL)}, \qquad (29a)$$

$$\Phi_j^{(NL)} = (1 - t_{ij}^2)^{1/2}\,\Omega_j^{(NL)} + t_{ij}\Omega_i^{(L)}, \qquad (29b)$$

and identified as 'natural localized molecular orbitals' (NLMOs).[36] More generally, each NLMO is the result of many such delocalizations from its NBO 'parent', viz.,

$$\Phi_i^{(L)} = t_{ii}\Omega_i^{(L)} + \sum_j t_{ij}\Omega_j^{(NL)},\ i = 1, 2, \ldots, N/2, \qquad (30a)$$

$$\Phi_j^{(NL)} = t_{jj}\Omega_j^{(NL)} + \sum_i t_{ji}\Omega_i^{(L)},\ j = N/2. \qquad (30b)$$

By construction,[36] each L-type NLMO is the *least delocalized* ('most NBO-like') orbital that recovers full double-occupancy, which in turn insures that NLMOs are unitarily equivalent to canonical MOs in the sense of Fock's theorem.[37] This means that NLMOs are *equally valid* orbitals for constructing or interpreting the HF/DFT wavefunction, density, or any other observable property of the system, and perceived 'physical differences' between

  

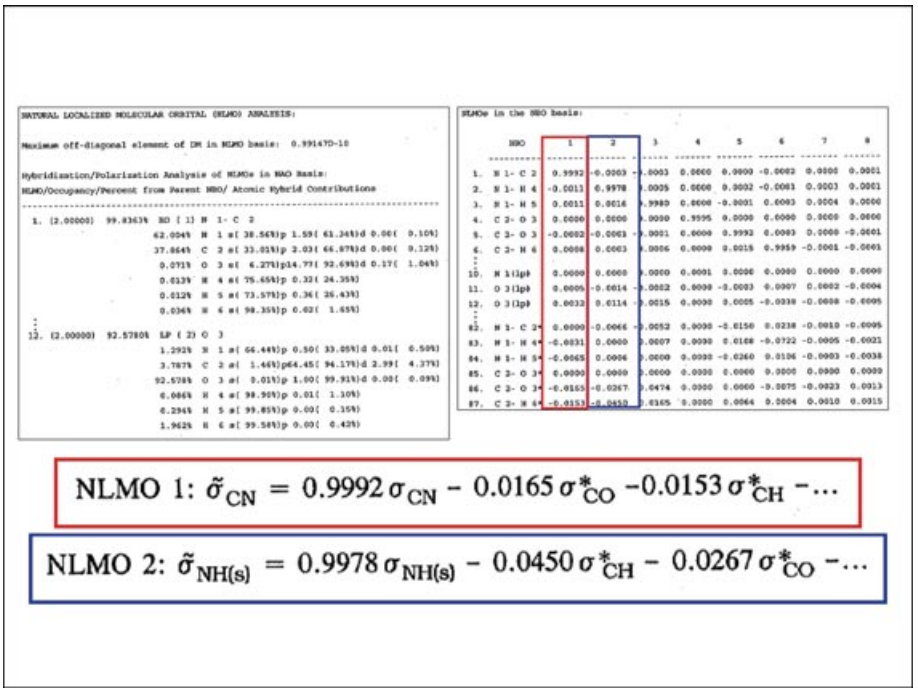


**FIGURE 27** | Natural bond orbital (NBO) compositions of $\sigma_{CN}$, $\sigma_{NH}$ 'natural localized molecular orbitals' (NLMOs) of formamide, showing dominant Lewis-type 'parent' and leading non-Lewis-type 'delocalization tails' of each NLMO.

NLMO-based and MO-based analyses are mathematically illusory.[38] In this sense, NLMOs represent the 'missing link' between localized NBO-based (Lewis-like) and delocalized MO-based concepts in single-determinant HF/DFT theory. Moreover, NLMOs of both L- and NL-type can be obtained analogously for post-HF wavefunctions, where their nondegenerate occupancies confer uniqueness properties not shared by other 'LMOs'. The NLMOs therefore provide an important addition to the NBO toolkit, underlying analysis of NMR chemical shielding (NCS keyword),[39] J-coupling (NJC keyword),[40] and other electronic properties.

Figure 27 illustrates how formamide NLMOs are displayed in program output. The boxed output at the left (from NLMO keyword) displays the percentage contribution of the dominant parent NBO (e.g., 99.84% $\sigma_{CH}$ NBO for NLMO 1), followed by atomic contributions to the weak 'delocalization tail' from other centers. The boxed output at the right (from NBONLMO keyword) expresses each NLMO in the form (30a,b) as a linear combination of NBOs, illustrated for the first two NLMOs at the bottom of the figure.

What about the alternate dipolar iminolate-like ($H_2N^+ = CHO^-$) resonance form of formamide? For this (or any other) proposed resonance structure, we can ask the program to find optimal NBOs of the bonding pattern requested by a \$CHOOSE keylist, as illustrated in Figure 28. The panel at the left displays the \$CHOOSE ... \$END input syntax for the dipolar resonance structure of formamide, and the panel at the right shows a portion of resulting \$CHOOSE output. As seen at the bottom of this panel, the best possible dipolar NLS has non-Lewis 'error' of 0.774e, whereas the corresponding error for the default formylamine NLS is 0.458e (Figure 22). Hence, the default NLS is indeed 'better' than the alternative dipolar form, as experimental evidence suggests.[41]

As is well known, the possible role of resonance of the form

(31)

was suggested by the planarity, high torsional barrier, and other anomalous structural features of amides. Consistent with such reasoning, we conjecture that an idealized formylamine NLS **I** *lacking* $n_N \rightarrow \pi^*_{CO}$ resonance delocalization would revert to the characteristic nonplanar, low-barrier structure of simple aminoalkanes. Fortunately, the NBO program, when linked to a suitable ESS host such as Gaussian,[42] includes powerful \$DEL ('delete') keylist capabilities for carrying out just such a *Gedankenexperiment*. As illustrated in Figure 29, the \$DEL keylist can

  

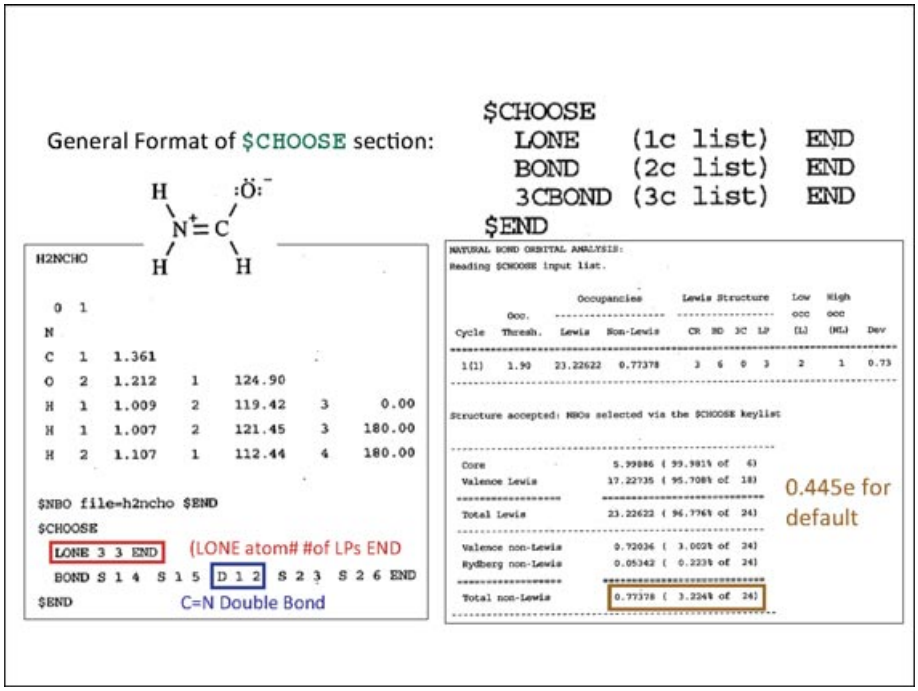


**FIGURE 28** | Illustrative input and output for $CHOOSE option to test alternative $N^{(+)} = C-O^{(-)}$ resonance structure of formamide.

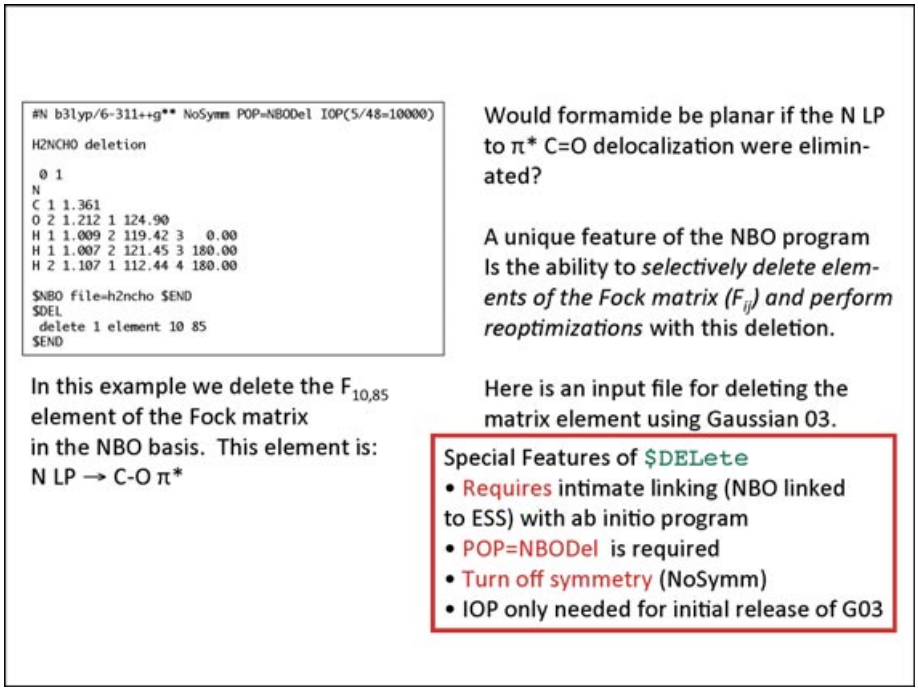


**FIGURE 29** | Illustrative $DEL keylist input to delete the leading $n_N \rightarrow \pi_{CO}^*$ (NBO 10 → 85) donor–acceptor interaction of formamide.

include commands to *delete selected donor–acceptor Fock matrix elements* (or entire NL-type NBOs, etc.) and recalculate the energy, geometry, and other properties in the *absence* of these interactions. In Figure 29, for example, the instruction 'delete 1 element 10 85' specifies removal of the 10 → 85 ($n_N \rightarrow \pi^*_{CO}$) donor–acceptor interaction that underlies amide resonance (31).

Figure 30 displays the first portion of NBO output for the $DEL input keylist of Figure 29. As seen in the 'change' column, deletion of the $F_{10,85}$ Fock matrix element reduces $n_N \rightarrow \pi^*_{CO}$ charge transfer

  

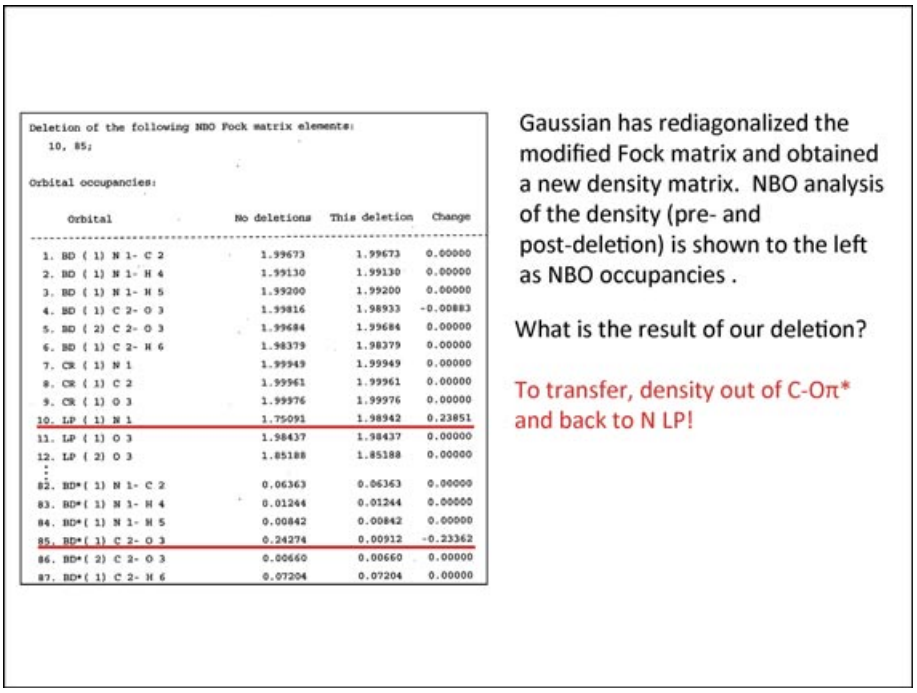


**FIGURE 30** | Output for $DEL deletion of Figure 29, showing restoration of occupancy in natural bond orbitals (NBOs) 10, 85 to near-idealized N—C═O Lewis structural form.

by ~0.23e, restoring $n_N$ to near-double occupancy (1.99e) and $\pi^*_{CO}$ to near-emptiness (0.01e). This confirms that $n_N$-$\pi^*_{CO}$ interaction is the 'smoking gun' responsible for the largest deviations from idealized NLS populations.

Energetic consequences of $DEL deletion are seen in the next output section (Figure 31), where the associated 'energy change' is evaluated as

$$\Delta E(\$\mathrm{DEL}) = 0.0985\ \mathrm{a.u.} = 61.8\ \mathrm{kcal/mol} \quad (32)$$

by a quasivariational approximation [In the single-pass SCF approximation, the general $\mathbf{F}[\rho]$ energy-evaluation functional is called only *once*, using the accurate Coulomb/exchange energetics of the fully converged $\mathbf{F}$ operator but the "unconverged" density $\rho_{\$DEL}$ requested by $DEL command. (Of course, allowing the SCF iterative procedure to cycle beyond the first pass would merely restore $\rho_{\$DEL}$ to original $\rho$ and $E$($DEL) to original $E$.)].Consistent with variational expectation, deletion of $n_N \rightarrow \pi^*_{CO}$ delocalization has *raised* $E$($DEL) by ~60 kcal/mol compared to $E$(SCF). This compares favorably with the perturbative estimate [E(2) ≅ 59.6 kcal/mol; Figure 25] of $n_N$-$\pi^*_{CO}$ stabilization. The $DEL procedure thereby offers a valuable quasivariational cross-check on second-order pertubative estimates of donor–acceptor energetics, partially incorporating higher-order coupling effects. The general correlation between $\Delta E$($DEL) and perturbative E(2) estimates is illustrated in Figure 32 for all significant donor–acceptor interactions of formamide.

As remarked above, energetic $DEL deletions can be combined with (numerical-gradient) optimization techniques to find the geometry of the idealized resonance-free NLS. For this purpose, the NOSTAR (delete all NL orbitals) command is employed, as shown in Figure 33. The figure includes the diagram of optimized NLS geometry and comparisons of NLS versus fully optimized geometrical parameters. As seen in these comparisons, the NLS reverts to the nonplanar geometry and near-ideal C—N, C═O bond lengths expected in the idealized Lewis structure limit.

A still more powerful tool for quantifying resonance-type phenomena is provided by 'natural resonance theory' (NRT)[43,44] This differs in many respects from the assumptions of Pauling's resonance theory (PRT),[45,46] but it leads similarly to probability-type 'resonance weights' $\{w_\alpha\}$ satisfying

$$0 \le w_a \le 1, \text{ each resonance structure } a, \quad (33a)$$

$$\sum_a w_a = 1, \quad (33b)$$

which can be applied in practically identical fashion to analysis and interpretation of experimental data. Like all NAO/NBO-based methods, NRT is applicable to

  

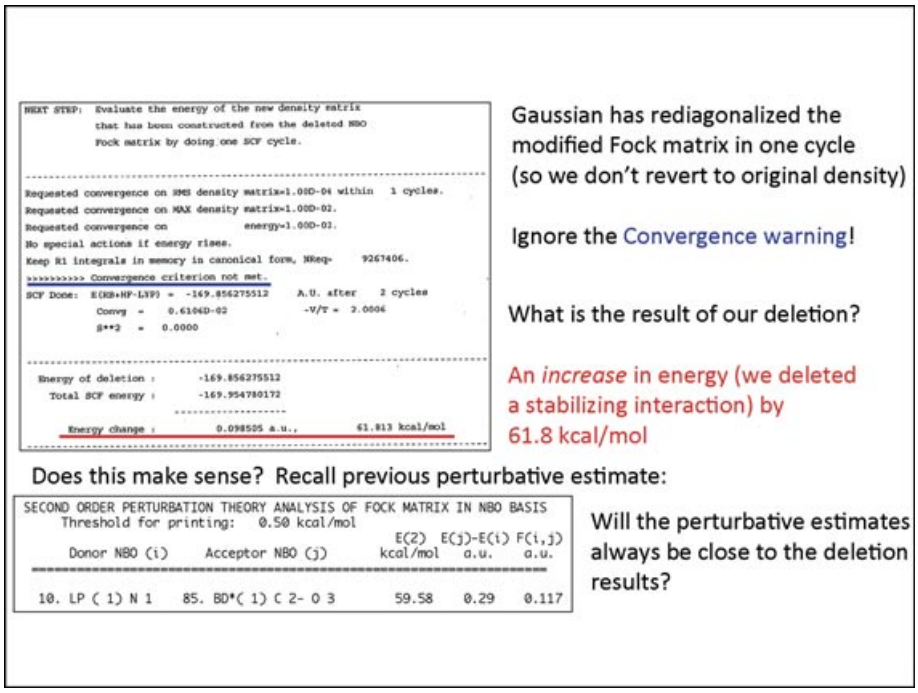


**FIGURE 31** | Further details of $DEL output (cf. Figures 29 and 30), comparing quasivariational deletion energy (61.81 kcal/mol) with corresponding perturbative E(2) estimate (59.58 kcal/mol).

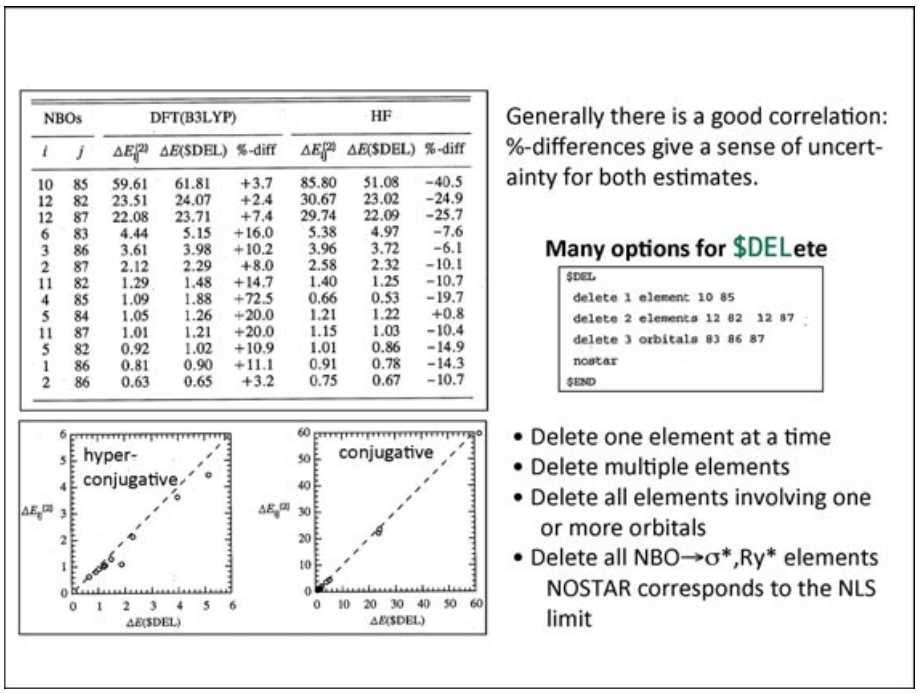


**FIGURE 32** | Table and graphs illustrating overall correlation between E($DEL) and E(2) estimates of donor–acceptor interaction strength.

HF or post-HF levels of any complexity (up to and including the *exact* wavefunction) and is based on variational density-maximization ('natural') criteria that allow strict quantification of residual error.

Figure 34 presents some concepts and nomenclature that underlie NRT algorithms (beyond the scope of full discussion in the present work) and displays a summary of NRT search results for

  

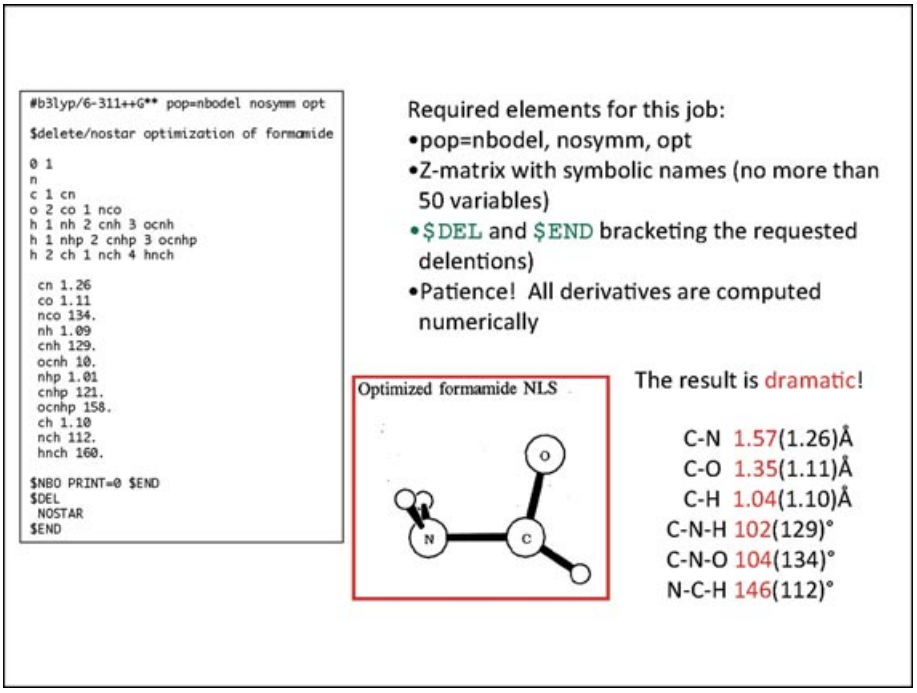


**FIGURE 33** | Illustrative $DEL input and resulting geometry for a 'nostar' ('delete all non-Lewis natural bond orbital (NBOs)' and associated resonance delocalizations) geometry optimization of formamide, showing reversion to pyramidalized amine group and near-ideal N—C, C═O bond lengths in the absence of amide resonance.

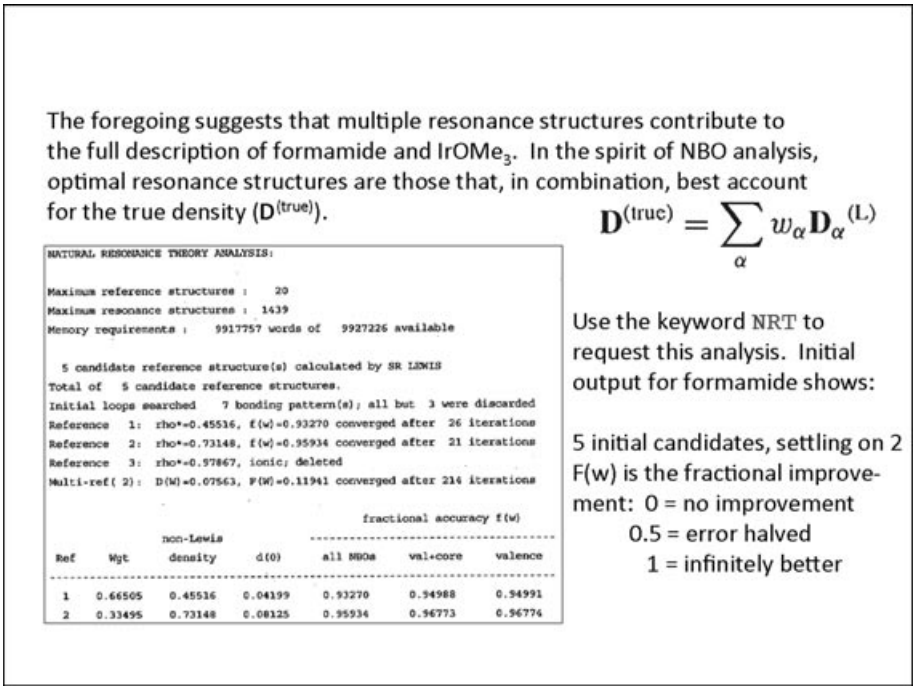


**FIGURE 34** | Outline of natural resonance theory (NRT) algorithm and sample output for formamide.

formamide. Figure 35 shows the table of NRT resonance weights and describes the cryptic notation for relating the primary resonance structure (specified by the atom–atom bonding table at the upper left) to each secondary structure. As seen at the right, the leading two structures are indeed those depicted in (31), with

  

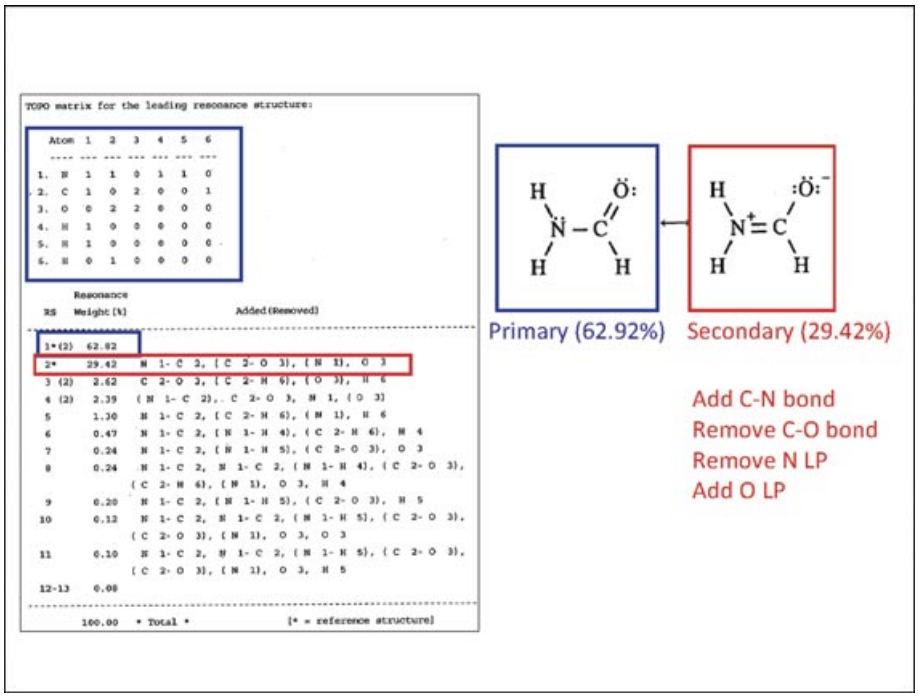


**FIGURE 35** | Further natural resonance theory (NRT) output for formamide (cf. Figure 34), showing weightings and structural bonding patterns for leading resonance structures.

relative weightings

$$w_{\mathrm{I}} = 62.8\%, \tag{34a}$$

$$w_{\mathrm{II}} = 29.4\% \tag{34b}$$

in good agreement with experimental estimates (e.g., $w_{\mathrm{I}} = 62\%$, $w_{\mathrm{II}} = 28\%$ in Ref 41).

The calculated NRT weightings for each bond pattern lead straightforwardly to the final NRT bond orders displayed in Figure 36. Each total (t) bond order $b_{\mathrm{AB}}$ is further divided into covalent (c) and ionic ('electrovalent') (i) contributions

$$\mathrm{b_{AB}} = \mathrm{b_{AB}^{(c)}} + \mathrm{b_{AB}^{(i)}} \tag{35}$$

according to the resonance-weighted ionicity factor (16) for each AB bond. The covalent $b_{\mathrm{AB}}{}^{(\mathrm{c})}$ component most nearly resembles older bond-order definitions employed by organic chemists (still displayed by the NBO BNDIDX keyword for backward compatibility), but only *total* $b_{\mathrm{AB}}$ exhibits the expected correlation with empirical structural data across a broad range of organic and inorganic species.

By summing the total NRT bond orders attached to given atom A, one also obtains the total atomic *valency* $V_{\mathrm{A}}$ (Sidgwick's 'combining power'), viz.,

$$V_{\mathrm{A}} = \sum_{\mathrm{B}} b_{\mathrm{AB}}, \tag{36}$$

which can again be separated into 'covalent' and 'electrovalent' contributions in analogous fashion. As shown in Figure 36, total NRT valency tends to be in excellent agreement with empirical periodicity assignments, viz., tetravalency of C ($V_{\mathrm{C}} = 4.00$), monovalency of H ($V_{\mathrm{C}} = 0.95$–$0.99$), etc.). A considerable body of evidence supports the superiority of NRT bond orders over older bond indices[47] for quantitative resonance-theoretic characterization of chemical phenomena.

## Transition Metal Species

Just as the striking stoichiometries of main-group $\mathrm{AL_n}$ compounds suggested the octet rule and related periodicity patterns for P-block elements (Figure 7), so can one infer analogous valency patterns from empirical regularities in $\mathrm{ML_n}$ stoichiometries for D-block elements, as summarized in Figure 37. Such regularities now suggest a *Rule of 12* ('duodectet rule'), governed by *six* D-block valence orbitals (presumably, one s + five d), analogous to the four P-block counterparts (one s + three p). From this starting point, one can envision idealized $\mathrm{sd}^{\mu}$ hybrids for transition metal bonding (analogous to $\mathrm{sp}^{\lambda}$ hybrids for main-group bonding), with minor 'polarization contributions' from nearby angular shells (viz., p-orbital contributions to $\mathrm{sd}^{\mu}$ hybrids, analogous to

  

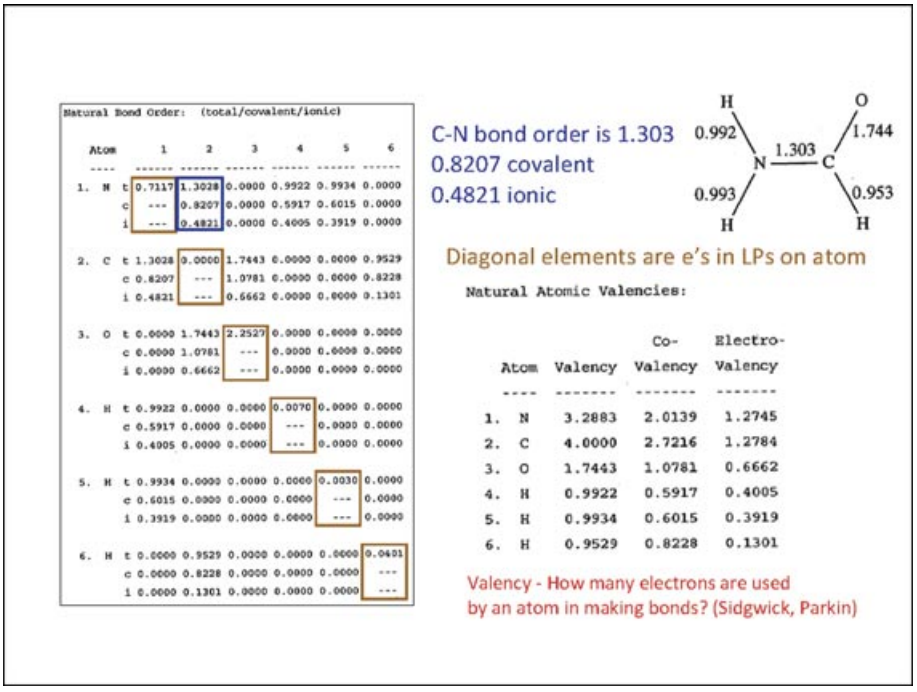


**FIGURE 36** | Further natural resonance theory (NRT) output for formamide (cf. Figures 34 and 35), showing covalent, electrovalent (ionic), and total contributions to NRT bond order and valency.

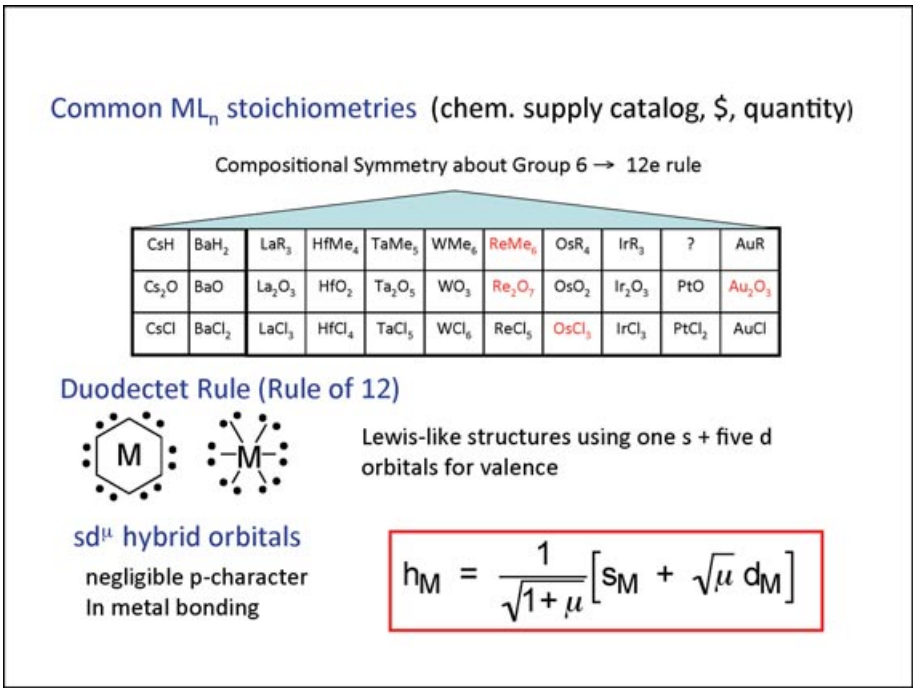


**FIGURE 37** | Similar to Figure 7, for transition metal bonding, showing Lewis-like 'duodectet rule' and hybrid formulations for D-block (sd$^\mu$-type) valence-shell bonding.

  

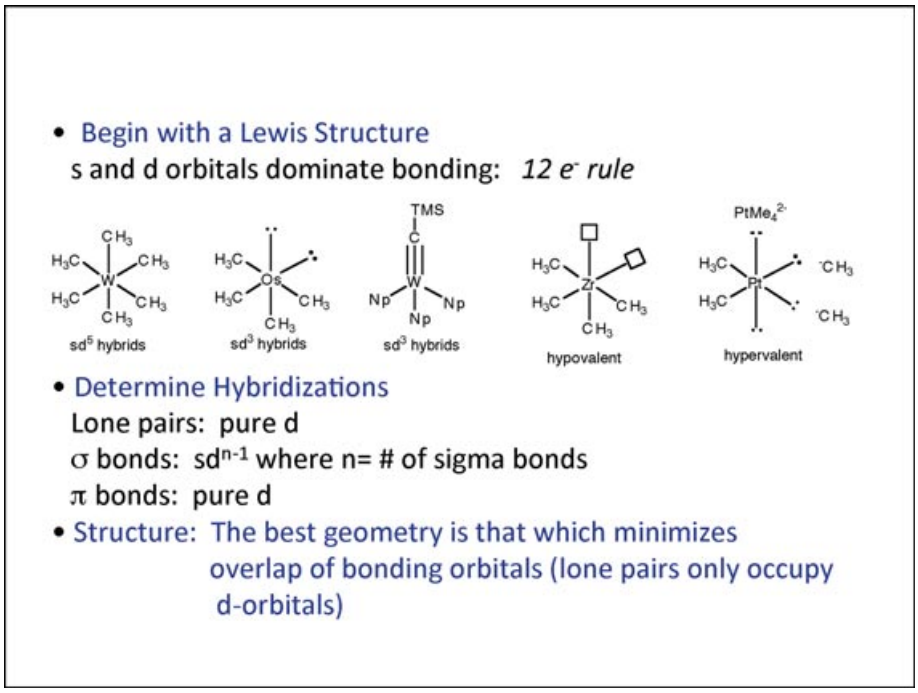


**FIGURE 38** | Lewis-like structures for transition metals, illustrating the 'Rule of 12' for idealized $sd^{\mu}$-type hybridized bonding.

d-orbital contributions to $sp^{\lambda}$ hybrids). In this generalization, Lewis-like dot diagrams typically have *hexagonal* (rather than square) arrangements of dot-pairs around each transition metal atom, as illustrated in Figure 38, but in other respects the mnemonic applications of such diagrams closely parallel those taught to generations of freshman chemistry students for main-group chemistry.

NBO analysis consistently exhibits such duodectet-conforming Lewis-like bonding patterns for transition metal species throughout the D-block. Figure 39 shows illustrative NBO output for $WH_6$, whose distinctly 'un-VSEPR-like' equilibrium structure is displayed in the ball-and-stick diagram. As the NPA charges and NBO hybridizations and polarization coefficients show, the six hydride bonds are not quite equivalent, but each exhibits essential covalency (low ionicity) and the near-ideal $sd^5$ hybridization expected for hexavalent tungsten. But why the oddly 'squashed' $C_{3v}$ geometry?

The equilibrium geometry of $WH_6$ actually conforms quite closely to that expected for idealized equivalent $sd^5$ NHOs, whose centrosymmetric forms are displayed in Figure 40. (The centrosymmetric character of $sd^{\mu}$ hybrids follows from the *gerade* symmetry of s and d orbitals of which they are composed.) The angle $\omega$ between equivalent $sd^{\mu}$ hybrids can be shown[48,49] to satisfy

$$\cos(\omega) = \pm[(\mu - 2)/(3\mu)]^{1/2}, \qquad (37)$$

which leads to *natural bond angles* shown in Figure 41, e.g.,

$$\theta = 63, 117 \quad \text{for } \mu = 5. \qquad (38)$$

It turns out[48,49] that idealized $sd^5$-$sd^5$ angles (38) can be simply related to vertices of an icosahedron in which *trans* arrangements are forbidden, leading to four possible idealized structures as depicted in Figure 41 (with that on the lower-right being of lowest energy for $WH_6$). Similar geometrical rationale can be given for other un-VSEPR-like bond angles calculated from Eq. (37), which is merely the D-block generalization of Coulson's directionality theorem [cf. Eq. (19)].

How well does the simple Lewis-like $sd^{\mu}$ picture describe accurately calculated transition metal species? Figure 42 shows NBO analysis results for third-row $MH_n$ transition metal hydrides $WH_6$, $ReH_5$,..., AuH. The results all confirm the high accuracy of the Lewis-like structure (99.56–99.98% $\rho_L$), the near-ideal $sd^{n-1}$ hybridizations, and the high covalency and occupancy (1.91–2.00e) of each MH bond. Indeed, the results are rather comparable to those for corresponding main-group species, showing that the Lewis-like picture is just as 'true' for $sd^{\mu}$-hybridized transition-metal bonding as for $sp^{\lambda}$-hybridized main-group bonding.

The strong analogies between main-group and transition-metal bonding extend also to formation

  

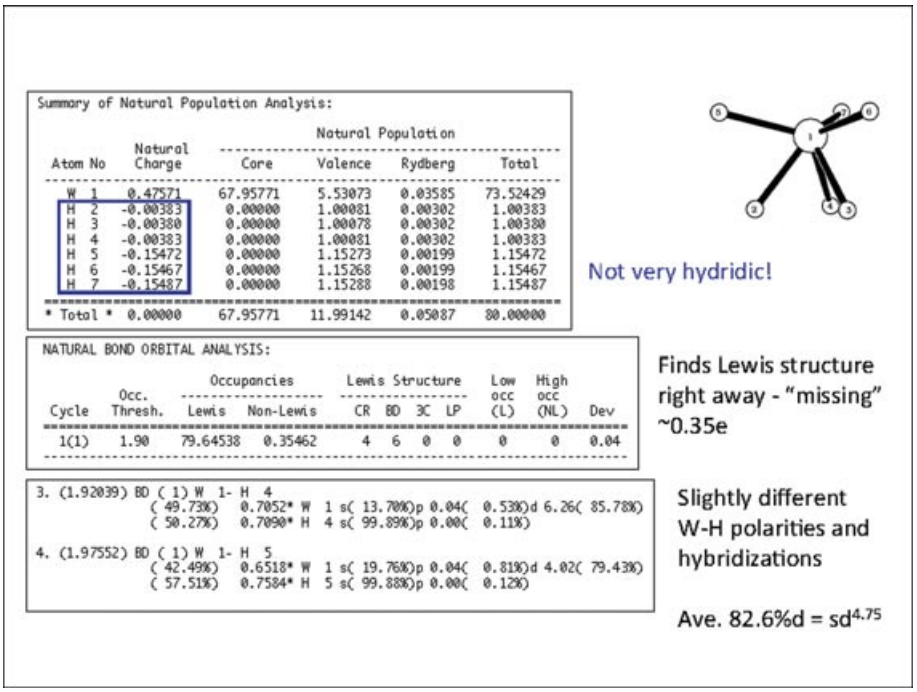


**FIGURE 39** | Sample natural population analysis (NPA)/natural bond orbital (NBO) output for $WH_6$, illustrating the near-ideal Lewis-like hybridization and bonding motifs for the strange-looking (non-VSEPR!) optimized ground-state geometry.

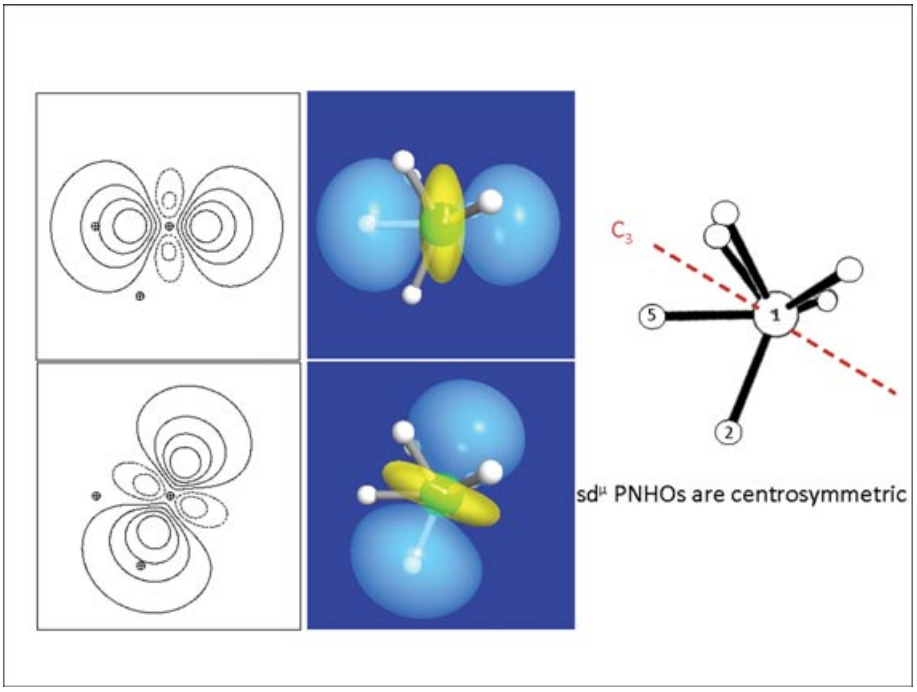


**FIGURE 40** | Bonding $sd^{\mu}$ hybrids for $WH_6$, illustrating centrosymmetric character of natural hybrid orbital (NHOs) and directional alignments with respect to nodal planes to achieve mutual orthogonality.

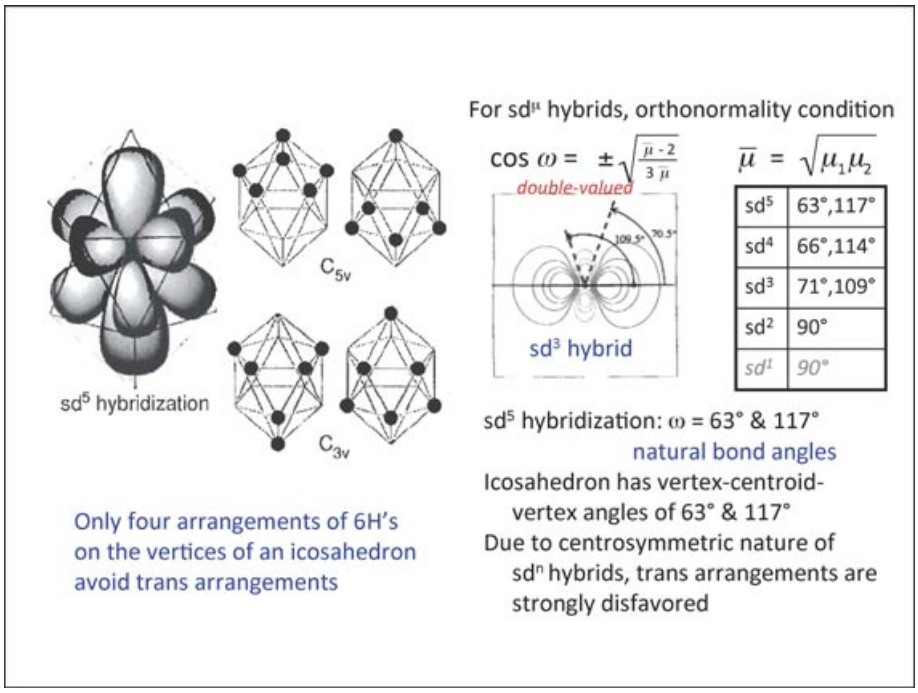


**FIGURE 41** | Further details of idealized $sd^{\mu}$ hybrids and bond angles for Lewis-like bonding of transition metals.

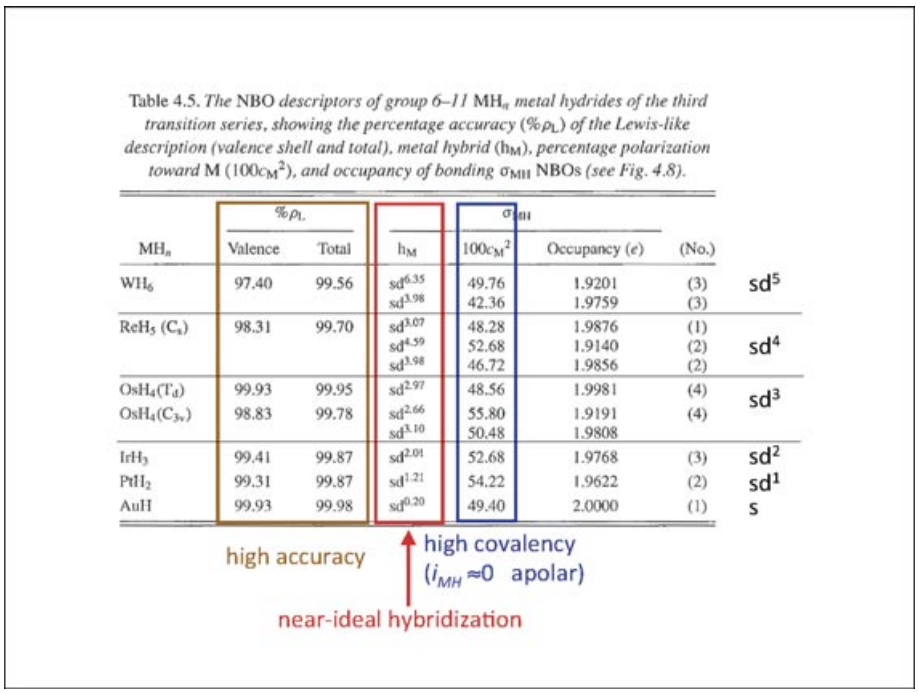

Table 4.5. *The* NBO *descriptors of group 6–11* $MH_n$ *metal hydrides of the third transition series, showing the percentage accuracy (*$\%\rho_L$*) of the Lewis-like description (valence shell and total), metal hybrid (*$h_M$*), percentage polarization toward* M ($100c_M^2$), *and occupancy of bonding* $\sigma_{MH}$ NBOs *(see Fig. 4.8).*

| | $\%\rho_L$ | | | $\sigma_{MH}$ | | | |
|---|---|---|---|---|---|---|---|
| $MH_n$ | Valence | Total | $h_M$ | $100c_M^2$ | Occupancy ($e$) | (No.) | |
| $WH_6$ | 97.40 | 99.56 | $sd^{6.35}$ | 49.76 | 1.9201 | (3) | $sd^5$ |
| | | | $sd^{3.98}$ | 42.36 | 1.9759 | (3) | |
| $ReH_5$ ($C_s$) | 98.31 | 99.70 | $sd^{3.07}$ | 48.28 | 1.9876 | (1) | |
| | | | $sd^{4.59}$ | 52.68 | 1.9140 | (2) | $sd^4$ |
| | | | $sd^{3.98}$ | 46.72 | 1.9856 | (2) | |
| $OsH_4$($T_d$) | 99.93 | 99.95 | $sd^{2.97}$ | 48.56 | 1.9981 | (4) | $sd^3$ |
| $OsH_4$($C_{3v}$) | 98.83 | 99.78 | $sd^{2.66}$ | 55.80 | 1.9191 | (4) | |
| | | | $sd^{3.10}$ | 50.48 | 1.9808 | | |
| $IrH_3$ | 99.41 | 99.87 | $sd^{2.01}$ | 52.68 | 1.9768 | (3) | $sd^2$ |
| $PtH_2$ | 99.31 | 99.87 | $sd^{1.21}$ | 54.22 | 1.9622 | (2) | $sd^1$ |
| AuH | 99.93 | 99.98 | $sd^{0.20}$ | 49.40 | 2.0000 | (1) | s |



**FIGURE 42** | Natural bond orbital (NBO) descriptors of group 6–11 $MH_n$ metal hydrides of the third transition series, showing percentage accuracy of Lewis-like description ($\%\rho_L$), metal hybrid ($h_M$), percentage polarization toward M ($100c_M^2$), and occupancy of $\sigma_{MH}$ NBOs.

of *multiple* bonds, but the richer valency palette (1–6) and enhanced $\pi$-type overlap of d-orbitals brings many surprising new bonding possibilities in D-block chemistry. For example, hexavalent tungsten easily forms dinuclear Lewis-like hydrides with *pentuple* metal-metal bonding (HW:::::WH), as displayed in Figure 43. The strongly trans-bent equilibrium geometry seems absurd from the viewpoint of VSEPR

  

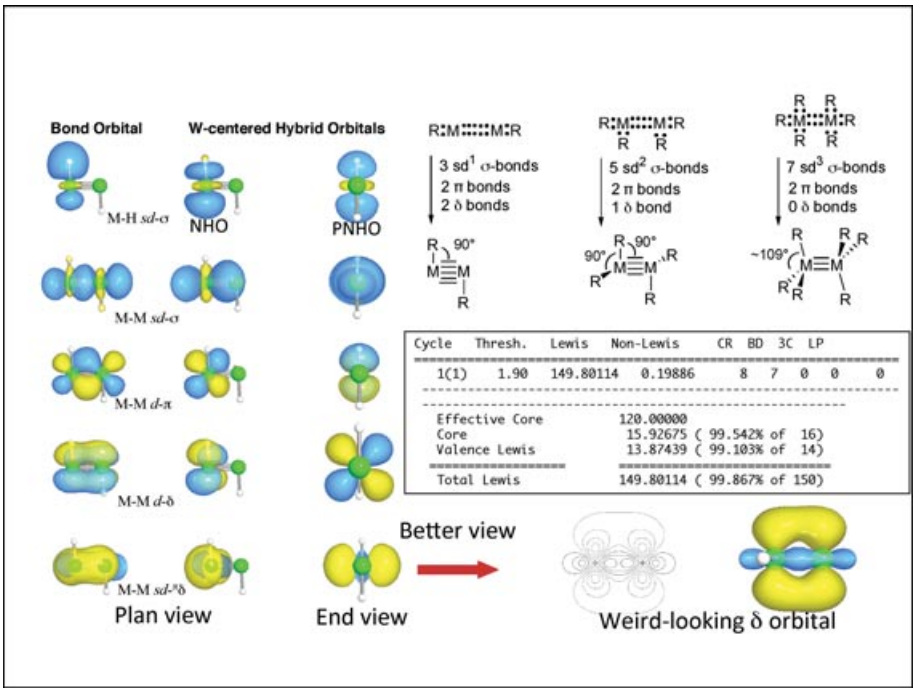


**FIGURE 43** | Duodectet diagrams and graphical forms of natural hybrid orbital (NHOs) and natural bond orbitals (NBOs) for high-order metal–metal multiple bonds in HWWH, $H_2WWH_2$, and $H_3WWH_3$.

theory (which actually gets most everything *wrong* in D-block bonding!), but is perfectly consistent with the expected 90° bond angles of ideal $sd^1$ skeletal hybridization [cf. Eq. (37)]. Despite the 'exotic' nature of high-order metal–metal bonding, the high accuracy of elementary Lewis-like description (99.87% $\rho_L$) is well preserved. As shown in Figure 43, similar remarks extend to quadruply bonded $H_2W{:::}WH_2$, triply-bonded $H_3W{:::}WH_3$, and other high-valency, high-bond-order species.

However, the centrosymmetric $sd^\mu$ bonding hybrids of D-block elements offer greatly enhanced tendency to coordinate additional ligands through so-called 3c/4e *hyper*bonding ('$\omega$-bonding') interactions.[50] As shown in Figure 44, each such 3c/4e L:···A···:L′$\omega$-bond can be formulated in terms of distinct L + AL′ and LA + L′ resonance structures:

$$\mathrm{L:\cdots A\cdots :L'} \equiv \mathrm{L:+A-L'} \longleftrightarrow \mathrm{L-A+:L'}, \tag{39}$$

*each* conforming to the 12e duodectet rule, but appearing in composite resonance-hybrid form as a 14e 'hypervalent' species. The NBO program provides automated search for strong 3c/4e interactions with the 3CHB (three-center hyperbond) keyword, as illustrated in Figure 44 for the trifluoride ion, $F_3^-$

$$\mathrm{F_3^-} \equiv \mathrm{F^- + F_2} \longleftrightarrow \mathrm{F_2 + F^-}. \tag{40}$$

Strong 3c/4e $\omega$-bonding is relatively uncommon in the P-block domain of directed $sp^\lambda$ hybrids, but becomes virtually *obligatory* in the D-block domain of centrosymmetric $sd^\mu$ hybrids where 'forward' or 'backward' interactions with coordinating ligands may be equally facile. In the presence of excess ligands, the steric constraints of a given transition metal center usually allow additional hyperbonded linkages (39) to form along *three* mutually perpendicular axes, thereby raising electron count from 12e to the familiar 18e limit in the final aggregated species.

As summarized in Figure 45, each 3c/4e hyperbond can be pictured as arising from a strong intermolecular donor–acceptor interaction of $n_L \rightarrow \sigma^*_{AL'}$ form (or $n_{L'} \rightarrow \sigma^*_{AL}$, in the alternative NLS representation). The equivalent NRT description is also shown in the figure, with each $F_3^-$ resonance structure in (40) contributing 43.6% to the resonance hybrid. Such interactions were originally described in the minimal-basis 'three-center MO' framework of Pimentel and Rundle,[51–55] which again demonstrates how the apparent hypervalency of $F_3^-$ and related main-group species can be achieved *without* 'd-orbital participation' or 'valence shell expansion'. Numerous computational studies have since established that essential structural features of $\omega$-bonded main-group species are well preserved even if d-type orbitals are *completely omitted* from the numerical basis set.[56–58]

  

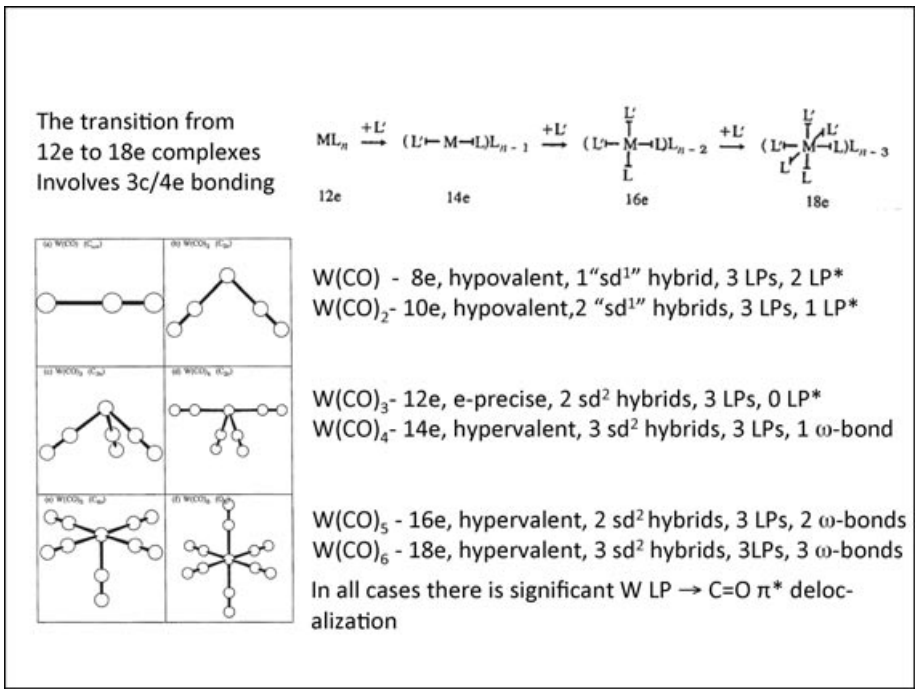


**FIGURE 44** | Successive carbonyl additions to tungsten, $W(CO)_n$, $n = 1$–6, showing Lewis-like coordination from hypovalent precursors ($n =$ 1,2) to normal-valent $W(CO)_3$ (12e, $C_{3v}$-symmetric), and thereafter to $W(CO)_6$ (18e, $O_h$-symmetric) by hypervalent 3c/4e aggregation.

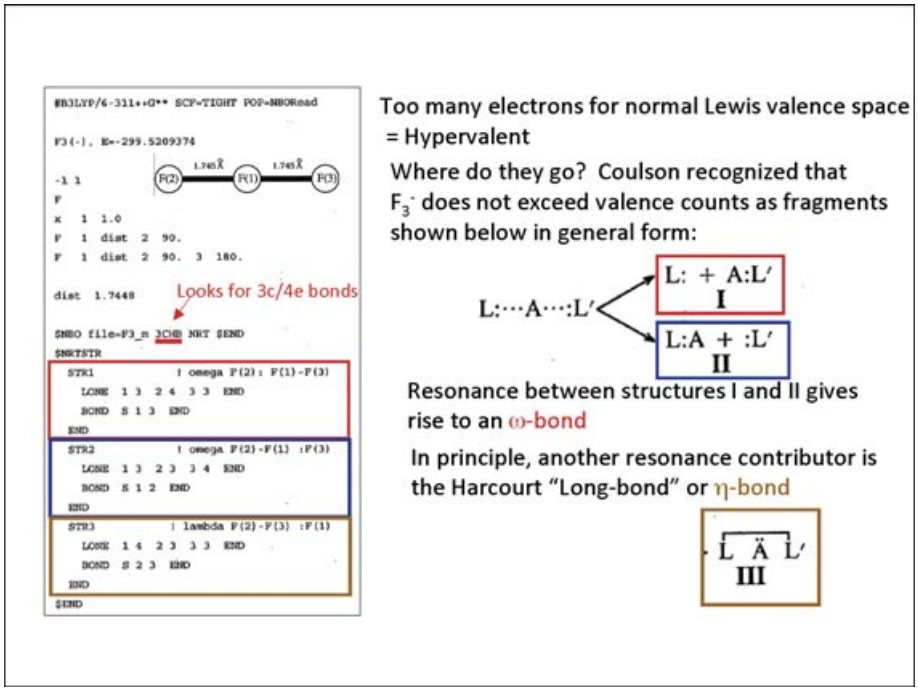


**FIGURE 45** | Sample $NRTSTR input for specifying 3c/4e hyperbonded resonance structures ($\omega$-bonded **I**, **II**; $\eta$-bonded **III**) for trifluoride ion ($F_3^-$), all within the framework of the octet rule.

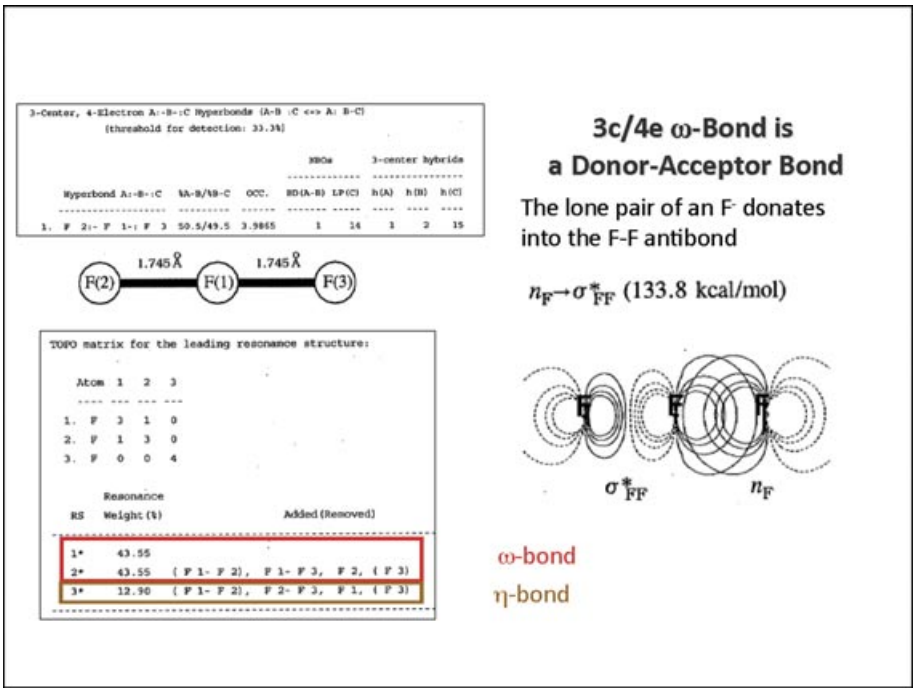


**FIGURE 46** | Natural resonance theory (NRT) description of 3c/4e hyperbonding in $F_3^-$, with associated $n_F \rightarrow \sigma_{FF}^*$ donor–acceptor diagram.

The final portion of NRT output for $F_3^-$ is presented in Figure 46, showing that adjacent F atoms are approximately 'half-bonded' ($b_{FF} \approx 0.44$), so that total valency ($V_F \approx 0.87$) of the central F atom remains comfortably within the nominal univalency of the halide family. As shown also in Figure 45, an unusual long-bond ('$\eta$-bonded') resonance structure is found to contribute at an appreciable level, conferring weak bond order (0.13) between *terminal* F atoms. (The NRT output thereby points to more exotic forms of 3c/4e $\eta$-bonding that apparently become more prominent in the metallic domain, but are beyond the scope of present discussion.) The $F_3^-$ example of Figures 44–46 serves to illustrate how NBO analysis provides multiple tools for characterizing more exotic 3c/4e (hypervalent) or 3c/2e (hypovalent) motifs beyond the standard 2c/2e Lewis structure diagram.

Figure 47 displays a more formal *Aufbau* diagram for NBO donor–acceptor interactions, showing how multicenter Lewis (2c, 3c,...) and non-Lewis (2c*, 3c*,...) NBOs can arise from starting single-center donor (1c) and acceptor (1c*) orbitals through successive donor–acceptor interactions. In this manner, conventional 2c/2e bonds are seen to represent only the first in a possible *heirarchy* of multicenter bonding interactions that may appear in diverse chemical species. As described below, forthcoming developments in NBO technology are expected to prove useful in exploring exotic new multicenter bonding motifs at the frontiers of modern chemical and materials research.

## Supramolecular Species

NBO methods provide strong support for the concept that 'chemical bonding forces' are not saturated by molecule formation, but extend to hydrogen bonding and other important 'fractional' bonding interactions that underlie supramolecular aggregation phenomena. This contradicts the assumptions of popular molecular dynamics (MD) empirical potentials that attempt to model H-bonding in terms of *classical* electrostatics–Coulombic interactions of atomic point charges, dipole-dipole forces, and the like.[59]

Let us return to the simple HF molecule, whose residual unfilled (acceptor, Lewis acid) valence shell capacity is described by the $\sigma^*_{HF}$ NBO of Figure 11. The principal donor (Lewis base) capacity of HF resides in its three valence lone pairs, particularly the two off-axis pure-p NBOs $n_F^{(x)}$, $n_F^{(y)}$ (Figure 10). Robust *inter*molecular $n_F \rightarrow \sigma^*_{HF'}$ donor–acceptor interactions can therefore be expected to stabilize dimer formation, as shown in the general resonance 'arrow pushing' diagram at the top of Figure 48. Indeed, the equilibrium $(HF)_2$ dimer is found to be bound by about 5 kcal/mol in the strongly bent (near L-shaped) geometry shown in the middle panel, quite *un*like the linear structure expected from classical dipole–dipole

  

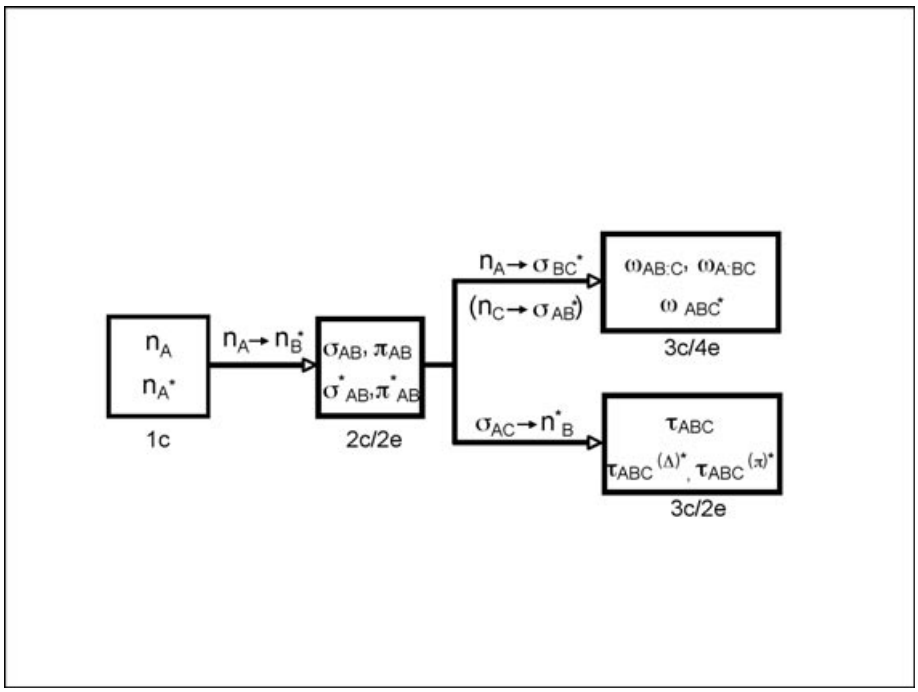


**FIGURE 47** | 'Natural bond orbital (NBO) Aufbau diagram' for multicenter delocalizations, showing leading steps of 2c/2e, 3c/2e (hypovalent), and 3c/4e (hypervalent) bond formation from starting 1c/1e hybrids.

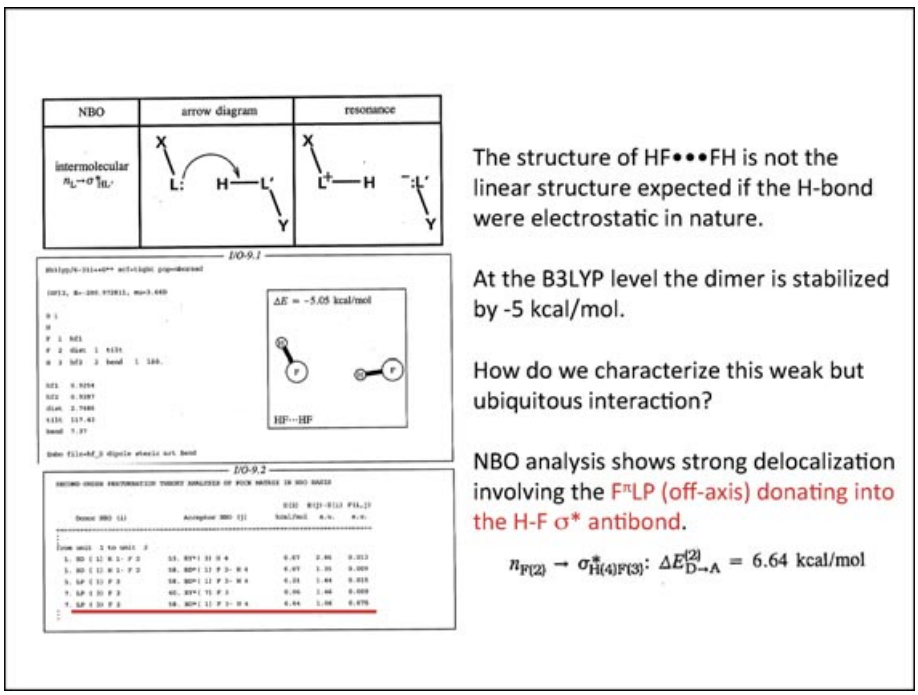


**FIGURE 48** | Mnemonic arrow-pushing and resonance structure diagrams for *inter*molecular donor–acceptor interactions (cf. Figure 26), with sample input and output for H-bonded $(HF)_2$ dimer.

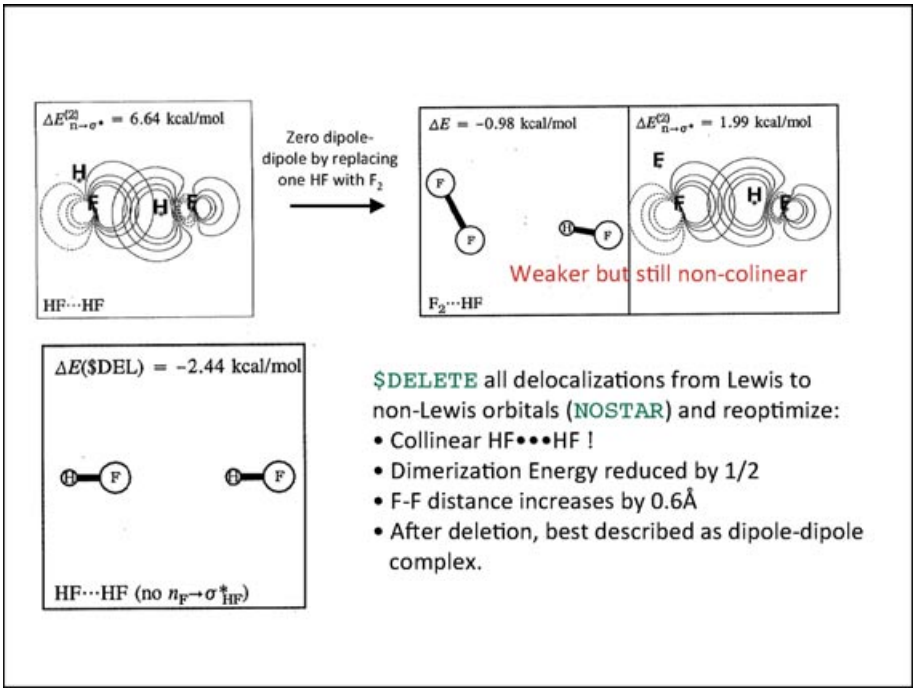


**FIGURE 49** | $DEL-reoptimization of $(HF)_2$ with intermolecular resonance-type $n_H \rightarrow \sigma_{HF}^*$ charge-transfer interaction deleted, showing reversion to a feeble, long-range 'dipole–dipole complex' having no resemblance to the actual H-bonded species.

attraction. The table of second-order E(2) values (bottom panel) confirms a strong intermolecular $n_F \rightarrow \sigma^*_{HF'}$ (NBOs 7 → 50) stabilization of 6.64 kcal/mol, with PNBO overlap diagram as shown at the upper left in Figure 49.

Consistent with freshman chemistry expectations, the donor $n_F$ and acceptor $\sigma^*_{HF}$ NBOs of $(HF)_2$ are found to be nicely aligned for near-maximal intermolecular overlap (although wrenched slightly out of exact L-shape by weaker dipole–dipole or steric forces favoring collinear alignment). Indeed, a very similar $n_F \rightarrow \sigma^*_{HF'}$ diagram is found for the related $F_2 \cdots HF$ complex (upper right of Figure 49), where the $F_2$ monomer *lacks* the dipole moment required for appreciable classical electrostatic interaction. In each case, the equilibrium $F \cdots HF'$ separation is well inside van der Waals contact distance, suggesting that $n_F \rightarrow \sigma^*_{HF'}$ attractions have successfully overcome significant steric repulsion to achieve the final geometry and net binding energy (as discussed below).

Further evidence that intermolecular $n_F \rightarrow \sigma^*_{HF}$ delocalization is indeed the 'smoking gun' primarily responsible for H-bond formation is displayed in the bottom panel of Figure 49. The panel shows the recalculated equilibrium geometry of $(HF)_2$ in the *absence* of intermolecular $n_F \rightarrow \sigma^*_{HF}$ delocalization, using the $DEL NOSTAR $END deletion procedure described previously (cf. Figures 29–31). As shown in Figure 49, the dimerization energy of the $DEL-complex (resonance-free NLS species) decreases by *half*, the monomer separation increases by ~0.6Å (to approximate van der Waals contact distance), and the angular geometry reverts to the collinear $HF \cdots HF$ alignment expected for a 'dipole-dipole complex'. Of course, the $DEL-deletion procedure leaves the monomer electron densities, dipole and higher multipole moments, and steric interactions virtually *unaltered* (up to >99.9% accuracy) at all distances, but it *qualitatively* alters the actual H-bond energetics and geometry. Similar results confirming the critical role of $n_B \rightarrow \sigma^*_{HA}$ charge transfer delocalization for H-bond formation are found in *all known* $B: \cdots HA$ complexes exhibiting the characteristic experimental signatures of H-bonding.

As indicated by the resonance mnemonic in Figure 48 (and confirmed by calculated NRT bond orders; see Ref 6, p. 187), the characteristic $n_B \rightarrow \sigma^*_{HA}$ donor–acceptor interactions of H-bonding all correspond to *fractional covalent bonding*, with calculated NRT bond orders in the range

$$0 \leq b_{BH} \leq 0.5 \qquad (41a)$$

and total (intraplus intermolecular) bond order satisfying

$$b_{HA} + b_{BH} \cong 1 \qquad (41b)$$

  

consistent with the two-resonance picture (39), (40). Of course, at the upper limit $b_{BH} = 0.5$ of (41a), one merely reverses what are called 'intra-' versus 'inter-', or 'covalent bond' versus 'H-bond'. H-bonding is thereby seen to be a *continuous fractional-bonding phenomenon* that passes seamlessly into the covalent bonding regime as the proton is 'half-transferred' from one Lewis base to the other.

The calculated NPA charges and other NAO/NBO descriptors also conform to the picture of continuously variable charge transfer between monomers as formal proton transfer progresses. The formal 'half-transferred' limit ($b_{BH} = b_{HA} = 0.5$) is achieved not only for strong symmetric equilibrium species such as $FHF^-$ or $H_5O_2^+$, but also for transition-state species in all proton transfer reactions, including the important 'low-barrier hydrogen bonds' (LBHB)[60,61] of enzymatic active sites. NBO methods also allow analysis of characteristic NMR and other spectroscopic signatures of LBHB phenomena, showing their direct relationship to NRT bond order, NPA charge transfer, and other NBO-based descriptors. The 'natural energy decomposition analysis' (NEDA)[62–64] method gives a more explicit partitioning of interaction energy into charge transfer, electrostatic, and other physical components.

[In this context it should be noted that alternative Morokuma, Bickelhaupt–Baerends, Block Localized Wavefunction (BLW), Absolute Localized Molecular Orbitals (ALMO), and related EDA methods[65–70] are all characterized by *overlap dependencies* that lead to sharp disagreements with NAO/NBO-based and other overlap-free methods. Such overlap-dependence intrinsically leads to ambiguity in assigning electronic overlap density to one atomic center or another, thus making identification of 'charge transfer' essentially arbitrary and subjective.[71–74] The unphysical aspects of overlap-dependent charge assignments (including probability nonconservation and negative or Pauli-violating 'populations') are widely recognized in the pathologies of Mulliken population analysis, but the equivalent pathologies are less obvious when only purported 'charge transfer energy' (rather than quantity of charge itself) is presented in EDA output. The overlap-sensitivity of EDA conclusions can be easily demonstrated by re-formulation in terms of NAOs or other overlap-free orbitals. Indeed, the recent ETS–NOCV ('extended transition state–natural orbital for chemical valence') method of Ziegler et al.[75] corrects for normalization and Pauli-violation errors by a simple AO symmetric orthogonalization procedure, and its conclusions are found to closely resemble those of NAO/NBO-based analysis. Additional methodological issues surround Mo's BLW–EDA,[69] which is tied to the original Heitler–London formulation of covalent bond formation with its demonstrated numerical failures[76] for systems other than $H_2$. Although studies based on BLW and other overlap-dependent EDA methods continue to appear in the literature,[77] their divergence with respect to overlap-free NAO/NBO analysis methods should be considered neither surprising nor informative. *Caveat emptor!*]

Figure 50 shows further details of the decomposition of total interaction energy $\Delta E(R)$ into Lewis $[\Delta E_L(R) = \Delta E_{\$DEL}(R)]$ and non-Lewis $[\Delta E_{NL}(R)]$ components at each F···F separation $R$ (all other variables being adiabatically optimized). The resonance-free $E_L$ is seen to be only feebly attractive at large $R$ [consistent with the linear 'dipole-dipole complex' found in $E_{\$DEL}$ re-optimization (Figure 48)], but becomes steeply repulsive near the expected distance of van der Waals contact. The NBO STERIC[78–80] keyword can be used to analyze more detailed aspects of the short-range steric repulsions that dominate $\Delta E_L(R)$ near $R_{eq}$. As shown in Figure 50, the attractive $E_{NL}$ component is able to overcome the repulsive $E_L$ component down to fairly small separation ($R > 2.3$Å), drawing the monomers in to the final equilibrium H-bond separation near $R_{eq} \cong 2.7$Å. The illustrated competition between repulsive $E_L$ and attractive $E_{NL}$ contributions to total interaction energy is representative of that found in *all known* H-bonded complexes.[81]

## WHAT IS NEW ON THE NBO HORIZON?

The foregoing examples illustrate some leading NBO methods implemented in the current program version, *NBO 5.9*. Former program releases [*NBO 1.0* (1980), *2.0* (1985), *3.0* (1990), *4.0* (1996), *5.0* (2001)] have each introduced new analysis options as well as algorithmic improvements on earlier methods. The forthcoming *NBO 6.0*[82] program responds to ongoing advances in *ab initio* computing technology and burgeoning demands of its user community by introducing major new methods, keywords, and ESS/NBO communication enhancements as well as numerous smaller consistency and reliability improvements throughout the code. We briefly list below some major new keywords and features of *NBO 6.0*:

### Natural Coulomb Electrostatics Analysis (NCE Keyword)

The NCE method combines NPA atomic charges with interatomic distances to evaluate the

  

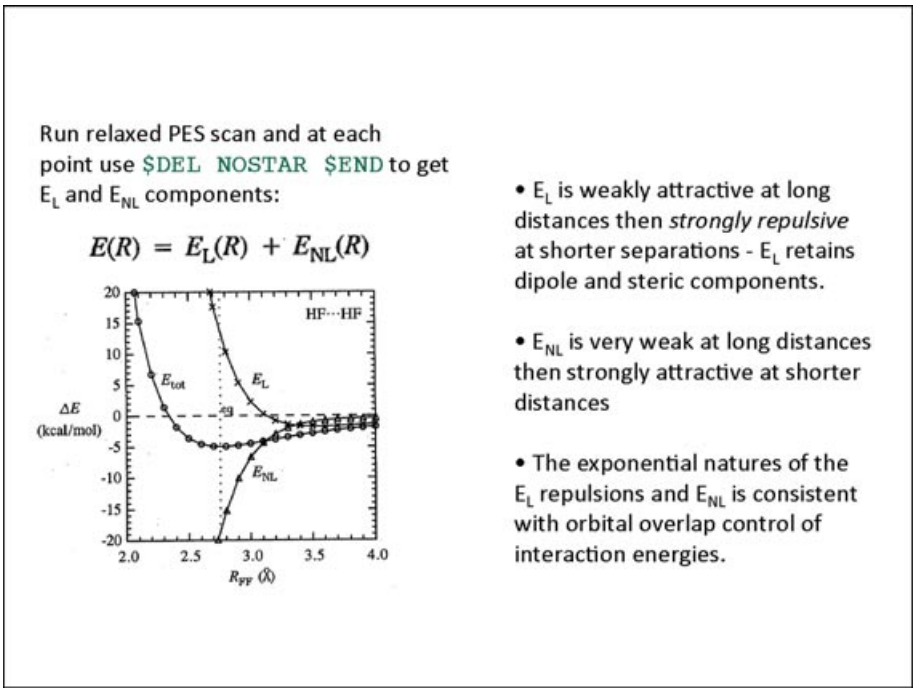


**FIGURE 50** | Potential curves for Lewis-type ($E_L$: steric, electrostatic), non-Lewis-type ($E_{NL}$: resonance-type charge transfer), and total interaction energy of $(HF)_2$ dimer, showing competition between exponentially varying $E_L$, $E_{NL}$ components that leads to the characteristic short bond length and anharmonic vibrational potential for the equilibrium H-bonded species.

classical-like 'point-charge Coulomb potential' that (although quantum mechanically unrealistic) makes contact with popular MD-type empirical potentials, including nonclassical L/NL contributions to intra- and intermolecular electrostatic interactions.

## Natural Cluster Unit Analysis (NCU Keyword)

The natural cluster unit (NCU) method[83] searches the density matrix for emergent cluster patterns as a 'temperature-like' atom–atom interaction threshold $t_{NCU}$ is continuously incremented from the weak-interaction (full aggregation) limit through successive regimes of supramolecular, molecular, and molecular fragmentation unit formation, up to the limit of fully disaggregated atomic fragments.

## General 1e Properties Analysis (PROP Keyword)

The PROP keyword allows NBO/NLMO-based localized analysis of *any* 1e property (kinetic energy, nuclear–electron attraction, electron density or any density-dependent property,...) for which the host ESS can provide matrix elements, expanding DIPOLE- or NJC-style options to an unlimited range of other properties.

## Multicenter NBO Search (NCBOND Keyword)

The NCBOND option automatically extends the NBO search to $n$-center bonding motifs up to $n = 9$, thereby deprecating previous 3CBOND (3c/2e) and 3CHB (3c/4e) specialized searches and opening up new vistas of (semi-)localized multicenter bonding in metallic and organometallic species.

## Improved ESS/NBO Communication Protocol

New ESS/NBO message-passing freeware allows ESS and NBO programs to perform highly interactive tasks (e.g., $DEL optimizations) *without* binary linking, thereby making full-fledged NBO methodology accessible to many additional ESS host programs.

## Improved Procedures for Excited-State Species

Strict new labeling conventions (i.e., '*' ≡ NL, whether or not 'out-of-phase') now make ground- and excited-state NBO analyses fully consistent, avoiding serious errors and oversights[84] of previous NLS searches for excited states, while also rationalizing L/NL labels for multicenter NBOs.

  

The present article has primarily focussed on NBO methods employed to analyze arbitrary wavefunctions input from the ESS, implying primary interprogram information flow from ESS to NBO. However, entirely different types of 'NBO methods' are based on employing NBO-type basis sets as fundamental building blocks for wavefunction *construction*, implying reversed program information flow from NBO to ESS. The latter methods take advantage of the localized nature of electron correlation[85] and include NBO-based variants of complete active space multiconfigurational SCF (CAS/NBO[86]) and coupled cluster (CC/NBO[87–89]) methods. Although such NBO-based methods are beyond the scope of present discussion, it is apparent that two-way 'link-free' ESS/NBO communication of *NBO 6.0* should facilitate such developments. Thus, future horizons of NBO research will likely focus on improved NBO-based strategies for obtaining accurate solutions of Schrödinger's equation, as well as improved analysis methods for relating such solutions to basic valency and bonding concepts.

## CONCLUSION

NBO methods enable rigorous analyses of electron densities computed with modern wavefunction technologies including restricted and unrestricted HF, DFT, MPn, etc. NBOs constitute an ideal 'chemist's basis set' that enables the wavefunction to be expressed in the language of localized Lewis-like electronic structures. Thus, NBO methods provide a vital link between the fundamental concepts of a chemical bond, Lewis dot structures, hybridization, resonance, and modern wavefunctions. Key to NBO description is the formulation of a complete, rigorously orthogonal set of NAOs. These orbitals underlie the analysis of atomic properties, such as atomic charge and electron configuration, within the molecular environment. From the NAOs and corresponding model, Hamiltonian, NHOs, and NBOs can be constructed and described in simple perturbative terms. Commonly understood bonding concepts such as bond order, hybridization, bond type (covalent, ionic, dative, $\sigma$, $\pi$, 2c-2e, 3c-2e, 3c-4e, etc), resonance, charge transfer, and sterics are revealed by NBO analyses of modern wavefunctions. The result is easily communicable chemical insight that extends from atoms to polyatomics to supramolecular species and spans the periodic table. New additions to the NBO program address improvements to *ab initio* computations through the introduction of new methods, keywords, and protocols for communication with electronic structure computation packages.

## REFERENCES


1. Lewis GN. The atom and the molecule. *J Am Chem Soc* 1916, 38:762.
2. Pauling L. The nature of the chemical bond. Application of results obtained from the quantum mechanics and from a theory of paramagnetic susceptibility to the structures of the molecules. *J Am Chem Soc* 1931, 53:1367.
3. Slater JC. Directed valence in polyatomic molecules. *Phys Rev* 1931, 37:481.
4. Coulson CA. *Valence*. 2nd ed. London: Oxford University Press; 1961.
5. Löwdin P-O. Quantum theory of many-particle systems. I. Physical interpretations by means of density matrices, natural spin-orbitals, and convergence problems in the method of configurational interaction. *Phys Rev* 1955, 97:1474.
6. Weinhold F, Landis CR. *Valency and Bonding: A Natural Bond Orbital Donor-Acceptor Perspective*. Cambridge: Cambridge University Press; 2005.
7. Almlöf J, Taylor PR. Atomic natural orbital (ANO) basis sets for quantum chemical calculations. *Adv Quant Chem* 1991, 22:301.
8. Reed AE, Weinstock RB, Weinhold F. Natural population analysis. *J Chem Phys* 1985, 83:735.
9. Mulliken RS. Electronic population analysis on LCAO-MO molecular wave functions. I. *J Chem Phys* 1955, 23:1833.
10. Sannigrahi AB, Nandi PK, Schleyer PvR. Ab initio theoretical study of the electronic structure, stability and bonding of dialkali halide cations. *Chem Phys Lett* 1993, 204:73.
11. Gross KC, Seybold PG. Substituent effects on the physical properties and p$K_a$ of aniline. *Int J Quant Chem* 2000, 80:1107.
12. Levine IN. *Quantum Chemistry*. 5th ed. Upper Saddle River, NJ: Prentice Hall; 2000, 169.
13. Weisskopf VF. Of atoms, mountains, and stars: a study in qualitative physics. *Science* 1975, 187:605.
14. Davidson ER. *Reduced Density Matrices in Quantum Chemistry*. New York: Academic; 1976.
15. Weinhold F. Natural bond orbital methods. In: Schleyer PvR, Allinger NL, Clark T, Gasteiger J, Kollman PA, Schaefer HF III, Schreiner PR, eds. *Encyclopedia of Computational Chemistry*, Vol. 3.


  

Chichester: John Wiley & Sons; 1998, 1792–1811.

16. For a comprehensive bibliography of recent NBO applications, see http://www.chem.wisc.edu/~nbo5/biblio.htm, NBO Bibliography. (Accessed May 18, 2011).
17. Pople JA, Beveridge DL. *Approximate Molecular Orbital Theory*. New York: McGraw-Hill; 1970.
18. R. Pauncz. *Alternant Molecular Orbital Method*. Philadelphia, PA: W. B. Saunders; 1967.
19. Hund F. The interpretation of complicated spectra, in particular those of the elements scandium to nickel. *Z Phys* 1925, 33:345.
20. Levine IN. *Quantum Chemistry*. 5th ed. Upper Saddle River, NJ: Prentice Hall; 2000, 328.
21. Mulliken RS. Electronic structures of molecules XI. Electroaffinity, molecular orbitals and dipole moments. *J Chem Phys* 1935, 3:573.
22. Jensen WB, *The Lewis Acid-Base Concepts*. New York: John Wiley & Sons, 1980, 74–77.
23. Pauling L, Wheland GW. The nature of the chemical bond. V. The quantum-mechanical calculation of the resonance energy of benzene and naphthalene and the hydrocarbon free radicals. *J Chem Phys* 1933, 1:362.
24. Wheland GW, Pauling L. A quantum mechanical discussion of orientation of substituents in aromatic molecules. *J Am Chem Soc* 1935, 57:2086.
25. Weinhold F, Landis CR. *Valency and Bonding: A Natural Bond Orbital Donor-Acceptor Perspective*. Cambridge: Cambridge University Press; 2005, 100–105.
26. Bent HA. An appraisal of valence-bond structures and hybridization in compounds of the first-row elements. *Chem Rev* 1961, 61:275.
27. Weinhold F, Landis CR. *Valency and Bonding: A Natural Bond Orbital Donor-Acceptor Perspective*. Cambridge: Cambridge University Press; 2005, 131ff.
28. Pauling L. The nature of the chemical bond. IV. The energy of single bonds and the relative electronegativity of atoms. *J Am Chem Soc* 1932, 54:3570.
29. Mulliken RS. Electronic structures of polyatomic molecules and valence. II. General considerations. *Phys Rev* 1932, 41:49.
30. Wolfsberg M, Helmholtz L. The spectra and electronic structure of the tetrahedral ions $MnO_4^-$, $CrO_4^-$, and $ClO_4^-$. *J Chem Phys* 1952, 20:837.
31. Hoffmann R. An extended Hückel theory. I. Hydrocarbons. *J Chem Phys* 1963, 39:1397.
32. Wendt M, Weinhold F. *NBOView 1.0, Theoretical Chemistry Institute*. Madison, WI: University of Wisconsin; 2001.
33. Weinhold F, Landis CR. *Valency and Bonding: A Natural Bond Orbital Donor-Acceptor Perspective*. Cambridge: Cambridge University Press; 2005, 91ff.
34. Weinhold F, Landis CR. *Valency and Bonding: A Natural Bond Orbital Donor-Acceptor Perspective*. Cambridge: Cambridge University Press; 2005, 16–20.
35. Weinhold F. Chemical bonding as a superposition phenomenon. *J Chem Ed* 1999, 76:1141.
36. Reed AE, Weinhold F. Natural localized molecular orbitals. *J Chem Phys* 1985, 83:1736.
37. Fock V. Näherungsmethode zur Lösung des quantenmechanischen Mehrkörperproblems. *Z Physik* 1930, 61:126.
38. See http://www.chem.wisc.edu/~nbo5/tutcmo.htm, MO vs. NBO–Tutorial Example. (Accessed May 18, 2011).
39. Bohmann JA, Weinhold F, Farrar TC. Natural chemical shielding analysis of nuclear magnetic resonance shielding tensors from gauge-including atomic orbital calculations. *J Chem Phys* 1997, 107:1173.
40. Wilkens SJ, Westler WM, Markley JL, Weinhold F. Natural *J*-coupling analysis: interpretation of scalar *J*-couplings in terms of natural bond orbitals. *J Am Chem Soc* 2001 123:12026.
41. Kemnitz CR, Loewen MJ. "Amide Resonance" correlates with a breadth of C–N rotation barriers. *J Am Chem Soc* 2007, 129:2521.
42. Frisch MJ, Trucks GW, Schlegel HB, Scuseria GE, Robb MA, Cheeseman JR, Scalmani G, Barone V, Mennucci B, Petersson GA, et al. *Gaussian 09*, Gaussian, Inc., Wallingford, CT, 2009.
43. Glendening ED, Weinhold F. Natural resonance theory. II. Natural bond order and valency. *J Comput Chem* 1998, 19:593, 610.
44. Glendening ED, Badenhoop JK, Weinhold F. Natural resonance theory. III. Chemical applications. *J Comput Chem* 1998, 19:628.
45. Pauling L. *The Nature of the Chemical Bond*. 3rd ed. Ithaca, NY: Cornell University Press; 1960.
46. Wheland GW. *The Theory of Resonance and its Applicationsin Organic Chemistry*. New York: John Wiley & Sons; 1955.
47. Bean GP. Application of natural bond orbital analysis and natural resonance theory to delocalization and aromaticity in five-membered heteroaromatic compounds. *J Org Chem* 1998, 63:2497.
48. Landis CR, Firman TK, Root DM, Cleveland T. A valence bond perspective on the molecular shapes of simple metal alkyls and hydrides. *J Am Chem Soc* 1998, 120:1842.
49. Weinhold F, Landis CR. *Valency and Bonding: A Natural Bond Orbital Donor-Acceptor Perspective*. Cambridge: Cambridge University Press; 372–387.
50. Weinhold F, Landis CR. *Valency and Bonding: A Natural Bond Orbital Donor-Acceptor Perspective*. Cambridge: Cambridge University Press; 281–306.

  

51. Pimentel GC. The bonding of trihalide and bifluoride ions by the molecular orbital method. *J Chem Phys* 1951, 19:446.
52. Rundle RE. Electron deficient compounds. II. Relative energies of "Half-Bonds". *J Chem Phys* 1941, 17: 671.
53. Rundle RE. Electron deficient compounds. *J Am Chem Soc* 1947, 69:1327–2075.
54. Rundle RE. Coordination number and valence in modern structural chemistry. *Rec Chem Prog* 1962, 23: 194.
55. Coulson CA. Nature of the bonding in xenon fluorides and related compounds. *J Chem Soc* 1964, 1964:1442.
56. Kutzelnigg W. Bonding in the higher major group elements. *Angew Chem Int Edn* 1984, 23:272.
57. Magnusson E. Hypercoordinate molecules of second-row elements: d functions or d orbitals? *J Am Chem Soc* 1990, 112:7940.
58. Reed AE, Weinhold F. On the role of d Orbitals in sulfur hexafluoride. *J Am Chem Soc* 1986, 108:3586.
59. Haile JM. *Molecular Dynamics Simulation: Elementary Methods*. New York: John Wiley & Sons; 1992.
60. Cleland WW, Krevoy MM. Low barrier hydrogen bonds and enzymic catalysis. *Science* 1994, 264:1887.
61. Frey PA. Low-barrier hydrogen bonds. *Science* 1995, 268:189.
62. Glendening ED, Streitwieser A Jr. Natural energy decomposition analysis: an energy partitioning procedure for molecular interactions with application to weak hydrogen bonding, strong ionic, and moderate donor–acceptor interactions. *J Chem Phys* 1994, 100:2900.
63. Schenter GK, Glendening ED. Natural energy decomposition analysis: the linear response electrical self energy. *J Phys Chem* 1996, 100:17152.
64. Glendening ED. Natural energy decomposition analysis: explicit evaluation of electrostatic and polarization effects with application to aqueous clusters of alkali metal cations and neutrals. *J Am Chem Soc* 1996, 118:2473.
65. Morokuma K. Why do molecules interact? The origin of electron donor–acceptor complexes, hydrogen bonding and proton affinity. *Acc Chem Res* 1977, 10:294.
66. Ziegler T, Rauk A. A theoretical study of the ethylene-metal bond in complexes between copper(1+), silver(1+), gold(1+), platinum(0) or platinum(2+) and ethylene, based on the Hartree–Fock–Slater transition-state method. *Inorg Chem* 1979, 18:1558.
67. Bickelhaupt FM, Baerends EJ. Kohn–Sham density functional theory: predicting and understanding chemistry. *Rev Comput Chem* 2000, 15:1.
68. Esterhuysen C, Frenking G. The nature of the chemical bond revisited. an energy partitioning analysis of diatomic molecules E2 (E = N-Bi, F-I), CO and BF. *Theor Chem Acc* 2004, 111:381.
69. Nakashima K, Zhang X, Xiang M, Lin Y, Lin M, Mo Y. Block-localized wavefunction energy decomposition (blw-ed) analysis of s/p interactions in metal-carbonyl bonding. *J Theor Chem Comput* 2008, 7:639.
70. Khaliullin RZ, Lochan R, Cobar E, Bell AT, Head-Gordon M. Unravelling the origin of intermolecular interactions using absolutely localized molecular orbitals. *J Phys Chem A* 2007, 111:8753.
71. Weinhold F, Carpenter JE. Some remarks on nonorthogonal orbitals in quantum chemistry. *J Mol Struct (Theochem)* 1988, 165:189.
72. Weinhold F. Rebuttal to the Bickelhaupt–Baerends case for steric repulsion causing the staggered conformation of ethane. *Angew Chem Int Ed* 2003, 42:4188.
73. Weinhold F, Landis CR. *Valency and Bonding: A Natural Bond Orbital Donor-Acceptor Perspective*. Cambridge: Cambridge University Press; 229–234.
74. See www.chem.wisc.edu/~nbo/tut neda.htm, NEDA Tutorial Example. (Accessed May 18, 2011).
75. Mitoraj MP, Michalak AM, Ziegler T. A combined charge and energy decomposition scheme for bond analysis. *J Chem Theory Comput* 2009, 5:962–975.
76. Norbeck JM, Gallup GA, Valence-bond calculation of the electronic structure of benzene. *J Am Chem Soc* 1974, 96:3386.
77. Mo Y. 'Computational evidence that hyperconjugative interactions are not responsible for the anomeric effect. *Nature Chem* 2010, 2:648–652.
78. Badenhoop JK, Weinhold F. Natural bond orbital analysis of steric interactions. *J Chem Phys* 1997, 107:5406.
79. Badenhoop JK, Weinhold F. Natural steric analysis: ab initio van der Waals radii of atoms and ions. *J Chem Phys* 1997, 107:5422.
80. Badenhoop JK, Weinhold F. Natural steric analysis of internal rotation barriers. *Int J Quant Chem* 1999, 72:269.
81. Reed AE, Weinhold F, Curtiss LA, Pochatko D. Natural bond orbital analysis of molecular interactions: theoretical studies of binary complexes of hydrogen fluoride, water, ammonia, molecular nitrogen, molecular oxygen, carbon monoxide, and carbon dioxide with hydrogen fluoride, water, and ammonia. *J Chem Phys* 1986, 84:5687.
82. Glendening ED, Badenhoop JK, Reed AE, Carpenter JE, Bohmann JA, Morales CM, Landis CR, Karafiloglou P, Schmidt JR, Weinhold F. *NBO 6.0 Manual, Theoretical Chemistry Institute*. Madison, WI: University of Wisconsin; 2010.
83. Zubarev DY, Boldyrev AI. Developing paradigms of chemical bonding: adaptive natural density partitioning. *Phys Chem Chem Phys* 2008, 10:5207.
84. Weinhold F, Kutateladze AG, eds. *Computational Methods in Organic Photochemistry: Molecular and*


  

*Supramolecular Photochemistry*. Boca Raton, FL: Taylor & Francis/CRC Press; 2005, 393–476.

85. Kutzelnigg W. Localization and correlation. In: Chalvet O, Daudel R, Diner S, Malrieu JP, eds. *Localization and Delocalization in Quantum Chemistry*. Dordrecht: Reidel; 1975, 143.
86. Nemukhin AV, Weinhold F. Natural bond orbitals in multiconfigurational expansions: local treatment of electron correlation in molecules. *J Chem Phys* 1992, 97:1095.
87. Flocke N, Bartlett RJ. Localized correlation treatment using natural bond orbitals. *Chem Phys Lett* 2003, 367:80.
88. Flocke N, Bartlett RJ. Correlation energy estimates in periodic extended systems using the localized natural bond orbital coupled cluster approach. *J Chem Phys* 2003, 118:5326.
89. Flocke N, Bartlett RJ. A natural linear scaling coupled-cluster method. *J Chem Phys* 2004, 121: 10935.

  